

ISSN 1621-3823
ISBN : 2-910015-79-3

*NOTES SCIENTIFIQUES ET TECHNIQUES
DE L'INSTITUT DE MÉCANIQUE CÉLESTE*

S108

INPOP17a planetary ephemerides

V. Viswanathan, A. Fienga, M. Gastineau and J. Laskar.



Abstract

Based on the use of Cassini radio tracking data and the introduction of LLR data obtained at 1064 nm, a new planetary ephemerides INPOP17a was built including improvements for the planet orbits as well as for Moon ephemerides. Besides new asteroid masses, new parameters related to the inner structure of the Moon were obtained and presented here. Comparisons with values found in the literature are also discussed. LLR Residuals reach the centimeter level for the new INPOP17a ephemerides.

1 Planetary ephemerides

INPOP17a is an upgraded version of the INPOP planetary ephemerides, fitted to LLR observations, and including new observations of Mars and Saturn deduced from MEX, Mars Odyssey and Cassini tracking ([19], [8]). Tables 11 and 12 resume the data samples and the obtained residuals with INPOP17a and the previous INPOP delivery, INPOP13c [5].

Thanks to the Mars and Saturn supplementary material, a better estimation of the Mars ephemerides appears in Table 11 and in Figure 1 as well as better consistencies between DE and INPOP ephemerides (see for example Table 2 and Figures from 13 to 20). The section 1.1 presents comparisons between INPOP17a, INPOP13c, DE430 ([8]) and the latest DE436 ephemerides ([7]).

Adjustment of the gravitational mass of the sun was performed as recommended by the IAU resolution B2 as well as the sun oblateness (J_2), the ratio between the mass of the earth and the mass of the moon (EMRAT). Estimated values are presented on Table 1.

Masses of planets as well as the procedure for estimating the asteroid masses perturbing the inner planet orbits are the same as in INPOP13c and INPOP13a. Comparisons between asteroid masses obtained with INPOP17a and values gathered in [3] and its updated version [2] are given and discussed in section 1.2.

1.1 Estimation of uncertainties

Figures 13 to 20 present the differences in right ascension, declination and geocentric distances between INPOP17a, INPOP13c, DE430 and DE436 over 120 years. Differences between INPOP17a, DE430 and DE436 for Mars, Jupiter and Saturn are reduced compared to the INPOP13c-DE430 differences. This can be explained by the addition of supplementary data set deduced from Mars orbiter tracking data (see Fig. 1) and by an improvement (see Fig. 2) in the reduction procedure for the Cassini normal points reprocessed by JPL ([8]). The comparisons between INPOP17a, DE430 and DE436 give then an estimation of the ephemerides uncertainties induced by the use of different procedures of data analysis and of weighting schema. The differences INPOP17a-INPOP13c give internal uncertainties between to ephemerides based on the same dynamical modeling. All these uncertainty estimations are given in Table 2 and 3. In comparison to the INPOP delivery dedicated to the GAIA mission (INPOP10e, [6]), one can see that the differences on the Earth positions and velocities in the BCRF between INPOP solutions and the DE modeles are smaller even if the INPOP17a-DE430 differences is 30% more important than the INPOP13c-DE430. This can be explained by the changes induced on the Saturn orbit and the different number of fitted asteroid masses between INPOP (168) and DE430 (345).

1.2 Asteroid masses

168 asteroid masses are fitted in INPOP17a, representing an increase of 28 supplementary objects compared to the INPOP13c modele. Among them, 18 masses were obtained in using an *a priori sigma* based on published values gathered by [3] and [2]. The *a priori sigma* is taken as 3 times the published uncertainties.

No asteroid ring is considered neither INPOP17a nor in INPOP13c. Comparisons between the 168 asteroid masses obtained with the INPOP17a fit and masses collected by [3] and its update[2] are presented in Tables 13, 14, 15 and in Figure 3. On Tables 13, 14, 15 are presented masses inducing perturbations greater than 1 meter on the Earth-Mars distance on a 1970 to 2020 period. Values obtained by DE430 are also presented for comparisons.

On Figure 3, two plots are presented : one comparing masses obtained with INPOP17a masses deduced for objects inducing perturbations greater than 7 meters over 40 years on the geocentric

Table 1: Values of parameters obtained in the fit of INPOP13c, INPOP10e, DE430 and DE436 to observations.

	INPOP13c $\pm 1\sigma$	INPOP17a $\pm 1\sigma$	DE430 $\pm 1\sigma$	DE436 $\pm 1\sigma$
$(\text{EMRAT}-81.3000) \times 10^{-4}$	(5.694 ± 0.010)	(5.719 ± 0.010)	5.690	5.68217
$J_2^\odot \times 10^{-7}$	(2.30 ± 0.25)	(2.295 ± 0.010)	2.11	NC
$\text{GM}_\odot - 132712440000 \text{ [km}^3 \cdot \text{s}^{-2}\text{]}$	(44.487 ± 0.17)	(42.693 ± 0.04)	41.9394	41.939377

Table 2: Maximum differences between INPOP17a, INPOP13c, INPOP10e and DE430 from 1960 to 2020 in in α, δ and geocentric distances.

Geocentric Differences	DE430 - INPOP13c 1980-2020			INPOP17a - INPOP13c 1980-2020			DE436 - INPOP17a 1980-2020		
	α	δ	ρ	α	δ	ρ	α	δ	ρ
	mas	mas	km	mas	mas	km	mas	mas	km
Mercury	1.1	0.6	0.242	0.39	0.41	0.052	0.30	0.36	0.094
Venus	0.5	0.17	0.025	0.47	0.42	0.053	0.23	0.33	0.008
Mars	0.5	0.4	0.129	0.72	0.73	0.145	0.50	0.41	0.115
Jupiter	6.8	10.7	3.25	3.5	4.6	2.068	2.55	2.85	2.069
Saturn	1.0	0.5	1.80	0.8	0.4	1.55	0.22	0.37	0.225
Uranus	36.7	33.4	522.751	75.4	47.3	348.7	60.7	66.0	263.2
Neptune	36.7	53.1	959.567	42.3	29.8	3328.3	45.5	55.6	3825.4
Pluton	119.0	75.3	2412.760	236.8	42.0	2634.9	118.0	97.1	1529.0

distances of Mars and one comparing INPOP17a masses obtained for smaller perturbers. For important perturbers, the obtained masses are consistent with the one obtained from different technics gathered by [2] when for small perturbers, an over-estimations in the INPOP17a masses can be noted compared to [2] and DE430. This can be explained by the number of asteroid masses that have been fitted in INPOP17a (168) in comparisons to the DE430 sample (343).

1.3 Conclusion

INPOP17a is an update version of INPOP planetary ephemerides, especially for the Saturn orbit because of the implementation of 10 years of Cassini range data provided by [8]. Improvement is

Table 3: Maximum differences between INPOP17a, INPOP13c, DE430 and DE436 from 1980 to 2020 in cartesian coordinates of the earth in the BCRS.

Earth Barycentric Differences	XYZ	VxVyVz
	km	mm.s ⁻¹
INPOP13c - DE430	0.3763	0.0467
INPOP17a - DE430	0.350	0.0513
INPOP10e - DE423	0.84	0.113

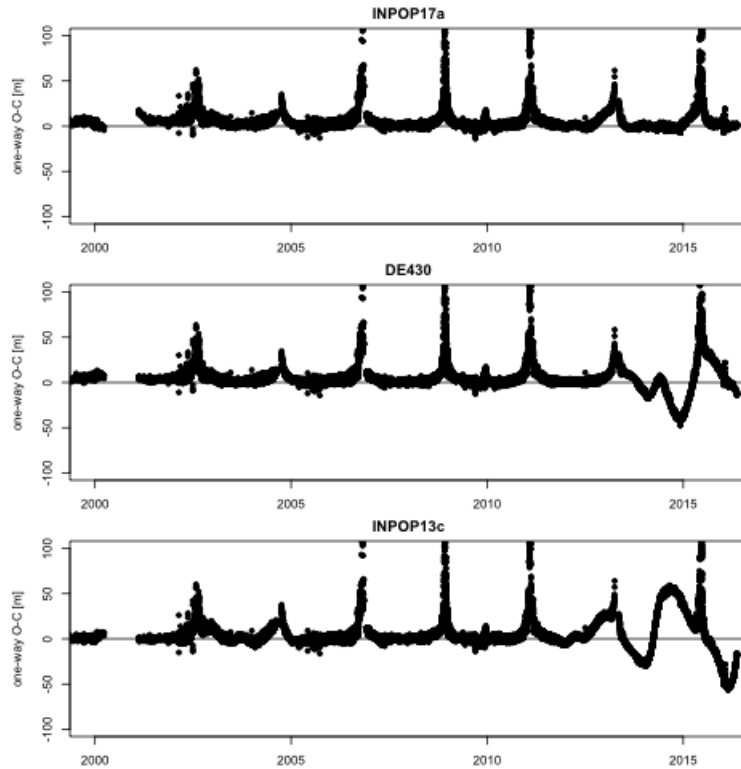


Figure 1: Residuals for MGS, MEX and Mars Odyssey one-way range in meters obtained with INPOP17a, DE430 and INPOP13c.

also noticeable for Jupiter orbit which become closer from DE430 than INPOP13c and for Mars orbit thanks to a better modeling of the solar conjunctions. 18 new asteroid masses have been estimated compared to INPOP13c and a better external accuracy is obtained for the BCRF Earth positions and velocities compared to the INPOP10e GAIA delivery. In the coming months, new inputs are expected : the Juno tracking data for a better constraint of the Jupiter orbit and a better estimate of the Jupiter mass and the Gaia DR2 publication of main belt asteroid positions. These latest are an important tool for improving the link between the GAIA reference frame and the INPOP reference frame when the former will be essential for a global improvement of the solar system orbital accuracy.

2 Lunar ephemerides

INPOP17a is fitted to LLR observations from 1969 to 2016, including new IR data obtained at the Calern station.

2.1 Lunar Laser Ranging

2.1.1 Principle

Lunar Ranging Retro Reflector (LRRR) arrays were part of the scientific payloads on the three US Manned (APOLLO XI, XIV, XV) and on-board two Soviet Rover (Lunakhod 1, 2) Lunar missions (hereby referred to as A11, A14, A15, L1 and L2 respectively). Arrays were installed by each respective mission, resulting in five distinct points but mainly equatorial on the near-side of the Moon (see Table 1). Retro-reflectors have the ability to reflect waves in the same direction as the incident waves, arising from the arrangement of the optical mirrors as a corner cube. This property,

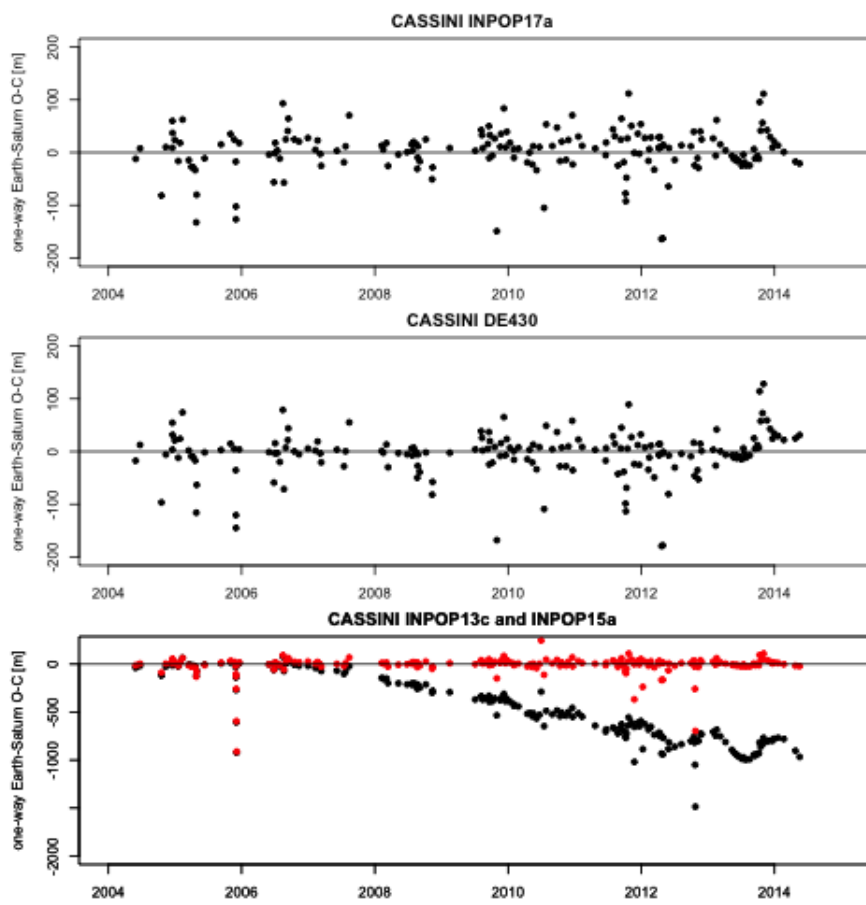


Figure 2: Cassini one-way range in meter obtained with INPOP17a, DE430 and INPOP13c.

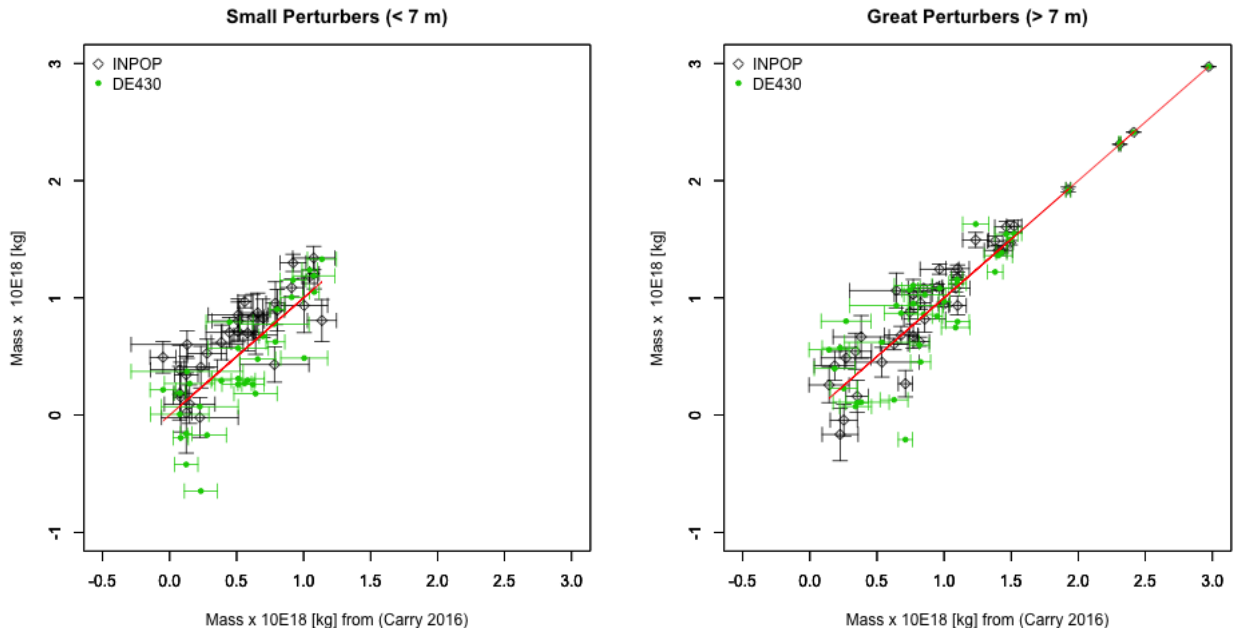


Figure 3: INPOP17a Asteroid mass determination. The x-axis is the log of masses extracted from [2] (as given in [12]) when the y-axis is the log of the INPOP and DE430 estimated masses in colors (see text). Right-hand side plot gathers masses of perturbers inducing perturbations smaller than 7 meters on the Earth-Mars distances over the interval from 1970 to 2010 (see [12]). Left-hand side plot gathers masses of perturbers inducing perturbations greater than 7 meters on the Earth-Mars distances.

along with the use of short-pulse lasers, state-of-the-art optical receivers and timing electronics, allows the measurement of the 2-way time of flight between a ground station on the Earth to each of the 5 retro-reflector arrays on the Moon, currently with millimeter precision.

The principle of the LLR observations is well documented ([24], [23]). Besides the lunar applications, this technique is still intensively used for tracking Earth orbiting satellites, especially for very accurate orbital ([28],[13]) and geophysical studies ([16], [10]).

The observational data used for the construction of the Moon dynamical modeling are not raw light time measurements. Each photon that is successfully captured by the detector is indeed characterized by an individual light time measurement. The real reflector returns are distinguished from the noise floor by correlating the distribution of the differences between observed light time and the simulated one with the shape of the laser pulse fired. Some modifications due to the tilt of the reflector array can also be considered ([18]). An iterative procedure described in ([27]) leads to one time of flight measurement per session, called a normal point associated with an observational accuracy combining signal over noise ratio, reflecting surface of the reflector, number of detected echos etc... This estimation of the observation uncertainty is related to the main characteristics of the tracking stations (diameter of the telescope, altitude of the site energy of the laser beam, etc...) as one can notice on the Grasse and APOLLO yearly evolution plotted on Fig. (7).

The historical LLR data spanning over 1969-2015 from all stations is available publicly in the "MINI" format at <http://polac.obspm.fr/llrdatae.html>. Recent LLR observations (both in Green and IR wavelength) from OCA is made available at <http://www.geoazur.fr/astrogeo/?href=observations/donnees/lune/brutes>.

Each LLR normal point contains information about the ground station (ITRF code), targets (lunar reflectors), time of flight of photons (s), observation epoch (UTC), meteorological measurements

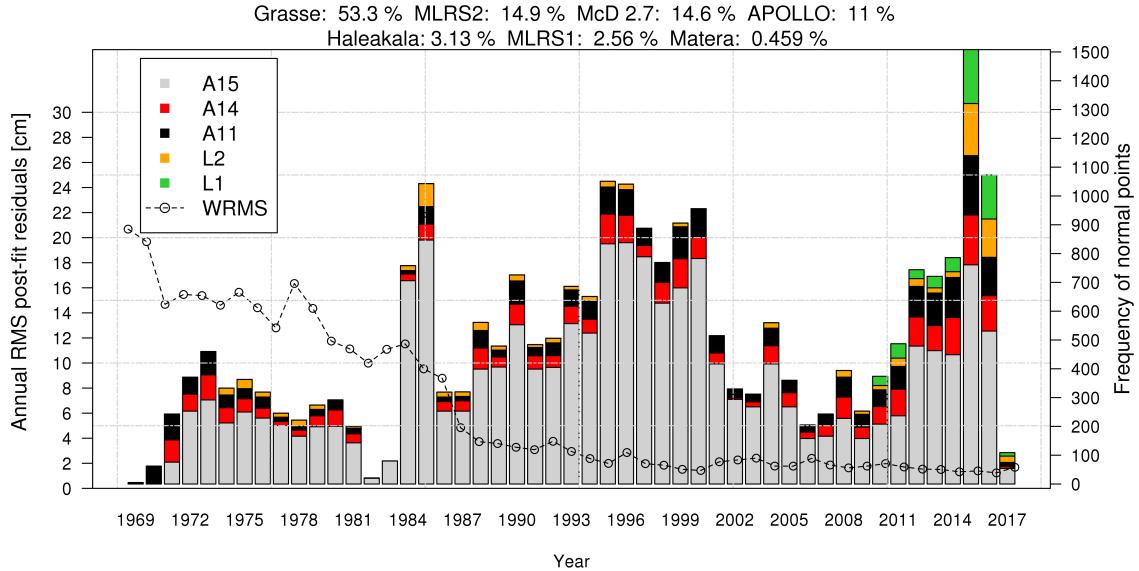


Figure 4: Histogram of annual frequency of LLR data with relative contribution from each LRR array including Grasse IR (1064 nm) observations. Points indicate the annual mean of post-fit residuals (in cm) obtained with INPOP17a. The dominance of range observations to A15 is evident. A change in paradigm can be noticed after 2014 due to the contribution from IR at Grasse.

at the ground station such as atmospheric pressure (0.01 *mbar*), ground temperature (0.1 °C) and relative humidity (%), wavelength of the laser used (0.1 *nm*) and data quality information through the number of echoes received, signal to noise ratio and the estimated uncertainties (0.1 *ps*).

2.1.2 Statistical distribution of LLR data

Non-uniform distributions in the dataset are one contributor to correlations between solution parameters ([36]). Like one can see on Fig. (4), Fig. (6) and Fig. (5), about 70% of the data are obtained after reflection on Apollo XV reflector arrays and in average 40 % of the data are acquired at 30° apart from the quarter moons.

In this study, we show how the IR LLR observations acquired at OCA during 2015-2017 (corresponding to 7% of the total LLR observations obtained between 1969-2017 from all known ILRS ground stations) can help for the reduction of such heterogeneity.

2.1.3 Spatial distribution

Statistics drawn from the historical LLR dataset (1969-2015) show an observer bias to range to the larger Apollo reflector arrays (mainly A15). This trend (see Fig. 4) is also present on statistics taken during time periods after the re-discovery of Lunakhod 1 by [21]. This is due to the higher return rate and thermal stability over a lunar day on the Apollo reflectors, thereby contributing to the higher likelihood of success.

With the installation of the 1064 nm detection path (see Fig. 6), as explained in ([4]), the detection of photon reflected on all reflectors is facilitated, especially for Lunakhod 2 (L2): about 17% of IR data are obtained with L2 when only 2% were detected at 532 nm.

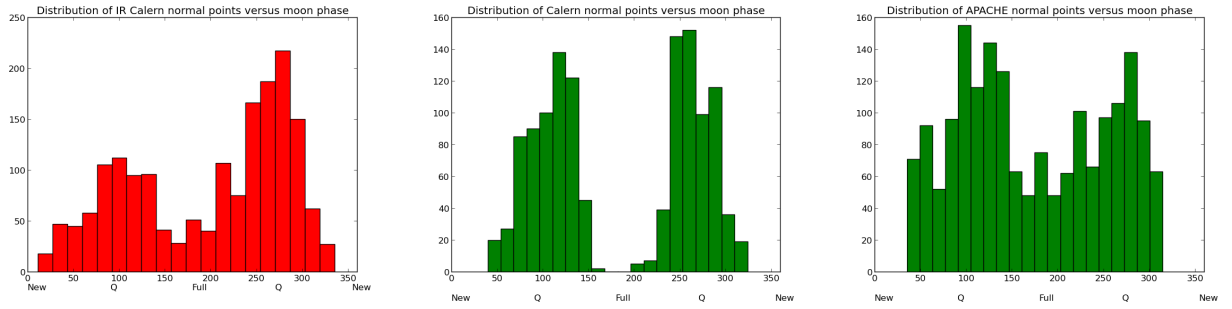


Figure 5: Histogram of synaptic distribution of normal points obtained at Apache Point (right-hand side), at the Calern station from 2012 from 2014 at 542 nm (center) and from 2014 to 2016 at 1064 nm (left-hand side).

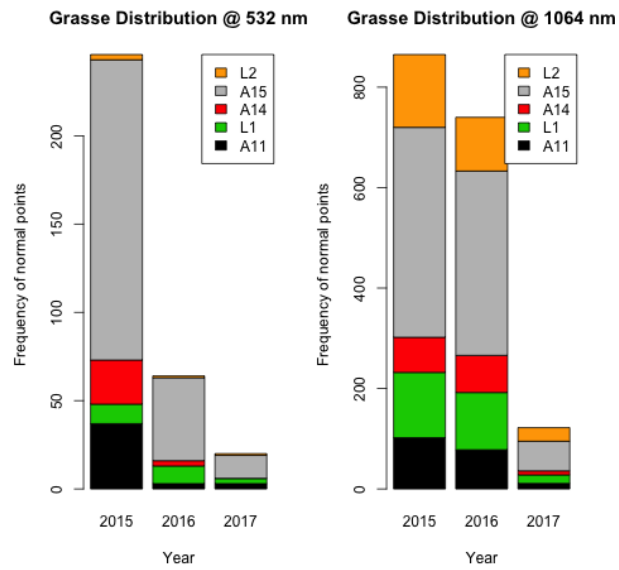


Figure 6: Grasse reflector wise distribution at 532 nm and 1064 nm from 2015 to 2017.

Owing to the spatial distribution of the reflectors on the Moon (see Table 1), Apollo reflectors offer principally longitude libration sensitivity at the Moon equator, whereas Lunakhod reflectors offer sensitivity both in the latitude and longitude libration of the Moon. The heterogeneity in the reflectore-wise distribution of LLR data affects then the sensitivity of the lunar modeling adjustment ([32]). By acquiring a better reflector-wise sample, IR contributes to improve the adjustment of the Moon dynamical and rotational modeling.

2.1.4 Temporal distribution

As demonstrated by [25], the full and new moon periods are the most favorable for testing gravity as the gravitational and tidal effects are maximum. On Fig. (5) are plotted the distributions of normal points relative to the synoptic angle for APOLLO and OCA station obtained at 532 nm and 1064 nm. When for the APOLLO data sets the distribution of normal point around quarter moons (15° before and after 90° and 270°) correspond to about 25% of the full data sample, almost 45% of the OCA 532 nm data sample is obtained away from the full and new moon periods. This can be explained by two factors:

- a. New Moon phase: As the pointing of the telescope onto the reflectors is calibrated with respect to a nearby topographical feature on the surface of the Moon, the pointing itself becomes a challenge when the reference points lie in the unlit areas of the Moon. Also, as the New Moon phase occurs in the daylight sky, the noise floor increases and the detector electronics become vulnerable due to ranging at a very close angle to the Sun ([4], [36]).
- b. Full Moon phase: During this phase, thermal distortions remain as the primary challenge, arising due to the over-head Sun heating of the retro-reflector arrays. This induces refractive index gradients within each corner cube causing a spread in the return beam, which makes detection more difficult. The proportion of this effect is partially linked to the thermal stability of the arrays. Since the A11, A14 and A15 arrays have a better thermal stability compared to the L1 and L2 arrays ([22]), observations to the latter become sparse during the full Moon phase.

Despite these challenges, LLR observations during the above mentioned phases of the Moon have been acquired with the IR detection. For the first two years of 1064 nm detection path at the OCA station, about 32% of observations were indeed obtained at 30° apart from the moon quarters, increasing by 10% the portion of data sample close from the most favorable periods for tides and EP studies.

This is primarily achieved due to the improved signal to noise ratio resulting from an improved transmission efficiency of the atmosphere at the IR wavelength of 1064 nm. In addition, high precision data have also been acquired on the two Lunakhod reflector arrays during full moon phase.

2.1.5 Observational Accuracy of LLR observations

APOLLO observations are obtained with a 3.5m telescope (under time sharing) at the Apache Point Observatory, while Grasse observations are obtained with a 1.5m telescope dedicated for LLR. A larger aperture is beneficial for statistically reducing the uncertainty of the observation, which translates to millimeter level accuracies as shown in Fig. (7) for APOLLO. This calls for an improvement of the Earth-Moon dynamical models within highly accurate numerically integrated ephemerides, as comparisons to dynamical models (solution SOL0 described in section 6.2) for APOLLO and Grasse stations at the level of about 1.5 cm.

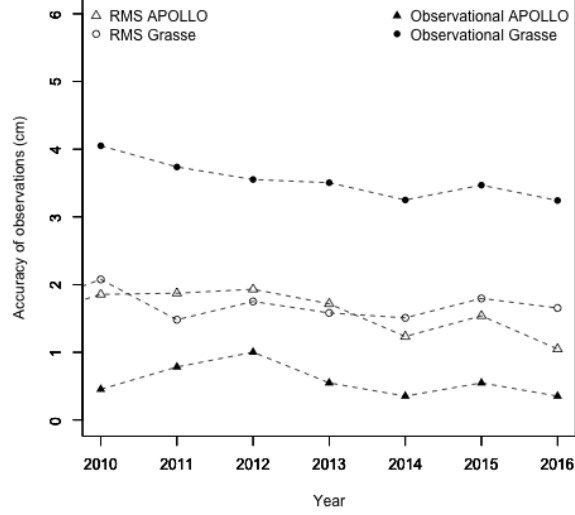


Figure 7: Accuracy of observation translated from annual mean of normal point uncertainty (in ps) to 1-way light time (LT) in cm, for APOLLO and Grasse LLR observations, compared with annual mean of post-fit residuals (1-way LT in cm) from Solution 1.

2.2 Lunar Dynamical Model

2.2.1 Lunar orbit interactions

In our model, we include the following accelerations perturbing the Moon's orbit:

1. Point mass mutual interactions from the Sun, planets and asteroids (through Eqn. 27 [9])
2. Point mass mutual interactions from the extended bodies (through Eqn. 28 [9]) which include :
 - the interaction of the zonal harmonics of the Earth through degree 6;
 - the interaction between zonal, sectoral, and tesseral harmonics of the Moon through degree 6 and the point mass Earth, Sun, Jupiter, Saturn, Venus and Mars;
 - the interaction of degree 2 zonal harmonic of the Sun.

3. Interaction from the Earth tides (through Eqn. 32 [9])

The tidal acceleration from the tides due to the Moon and the Sun are separated into three frequency bands (zonal, diurnal and semi-diurnal). Each band is represented by a potential Love number $k_{2m,E}$ with a matching pair of time delays $\tau_{Xm,E}$ (where subscript X is either associated with the daily Earth rotation $\tau_{Rm,E}$ or orbital motion $\tau_{Om,E}$) to account for frequency dependent phase shifts from an anelastic Earth with oceans. Here the time delay represents the phase lag induced by the tidal components. Although the time delay method inherently assumes that the real component of $k_{2m,E}$ varies linearly with frequency, it reduces the complexity of the dynamical model. The diurnal $\tau_{R1,E}$ and semi-diurnal $\tau_{R2,E}$ are included as solution parameters in the LLR analysis, while model values for potential Love numbers for a solid Earth are fixed to that from Table 6.3 in [29] followed by corrections from the ocean model FES2004 ([14]). A detailed explanation about the most influential tides relevant to the Earth-Moon orbit integration can be found in Table 6 in [34].

2.2.2 Lunar orientation and inertia tensor

1. Lunar frame and orientation The mantle coordinate system is defined by the principal axes of the undistorted mantle, whose moments of inertia matrix are diagonal. The time varying mantle Euler angles $(\phi_m(t), \theta_m(t), \psi_m(t))$ define the orientation of the principal axis (PA) frame with respect to the inertial ICRF2 frame (see [9] for details). The time derivatives of the Euler angles is defined through Eqn. 14 [9].
2. Lunar moment of inertia tensor

The undistorted total moment of inertia of the Moon \tilde{I}_T is given by:

$$\tilde{I}_T = \frac{\tilde{C}_T}{m_M R_M^2} \begin{bmatrix} 1 & 0 & 0 \\ 0 & 1 & 0 \\ 0 & 0 & 1 \end{bmatrix} + \begin{bmatrix} \tilde{C}_{2,0,M} - 2\tilde{C}_{2,2,M} & 0 & 0 \\ 0 & \tilde{C}_{2,0,M} + 2\tilde{C}_{2,2,M} & 0 \\ 0 & 0 & 0 \end{bmatrix} \quad (1)$$

where $\tilde{C}_{n,m,M}$ is the unnormalized degree n , order m of the Stokes coefficient $C_{n,m}$ for the spherical harmonic model of the undistorted Moon and \tilde{C}_T is the undistorted polar moment of inertia of the Moon normalized by it's mass m_M and radius squared R_M^2 . Through Eqn. (1), we are able to directly use the undistorted value of C_{22} ([15]) from GRAIL derived spherical harmonic model of [11].

The moment of inertia of the fluid core I_c is given by:

$$I_c = \alpha_c \tilde{C}_T \begin{bmatrix} 1 - f_c & 0 & 0 \\ 0 & 1 - f_c & 0 \\ 0 & 0 & 1 \end{bmatrix} = \begin{bmatrix} A_c & 0 & 0 \\ 0 & B_c & 0 \\ 0 & 0 & C_c \end{bmatrix} \quad (2a)$$

where α_c is the ratio of the fluid core polar moment of inertia C_c to the undistorted polar moment of inertia of the Moon \tilde{C}_T , f_c is the fluid core polar flattening and, A_c and B_c are the equatorial moments of the fluid core.

The moment of inertia of the mantle I_m has a rigid-body contribution \tilde{I}_m and two time varying contributions due to the tidal distortion of the Earth and spin distortion as given in Eqn. 41 of ([9]). The single time delay model (characterized by τ_M) allows for dissipation when flexing the Moon ([35], [31], [9]).

$$\tilde{I}_m = \tilde{I}_T - I_c \quad (2b)$$

3. Lunar angular momentum and torques

The time derivative of the angular momentum vector is equal to the sum of torques (N) acting on the body. In the rotating mantle frame, the angular momentum differential equation for the mantle is given by:

$$\frac{d}{dt} I_m \omega_m + \omega_m \times I_m \omega_m = N \quad (2c)$$

where N is the sum of torques on the lunar mantle from the point mass body A ($N_{M,figM-pmA}$), figure-figure interaction between the Moon and the Earth ($N_{M,figM-figE}$) and the viscous interaction between the fluid core and the mantle (N_{CMB}). The motion of the uniform fluid core is controlled by the mantle interior, with the fluid core moment of inertia (I_c) constant in the frame of the mantle. The angular momentum differential equation of the fluid core in the mantle frame is then given by:

$$\frac{d}{dt} I_c \omega_c + \omega_m \times I_c \omega_c = -N_{CMB} \quad (2d)$$

Table 4: LLR observations from ILRS ground stations with corresponding time span and number of normal points available, with the new IR dataset from Grasse in bold.

Code	Station	Time span [yyyy/mm/dd]	Normal points		INPOP WRMS [cm]
			Available	Used	
70610	Apache Point, NM, USA (group A)	2006/04/07 - 2010/10/30	941	929	1.27
70610	Apache Point, NM, USA (group B)	2010/12/01 - 2012/04/05	506	486	1.95
70610	Apache Point, NM, USA (re-group C)	2012/04/07 - 2013/09/01	361	345	1.52
70610	Apache Point, NM, USA (group D)	2013/09/30 - 2016/11/25	832	800	1.15
01910	Grasse, FR (693.8 nm Ruby laser)	1984/04/07 - 1986/06/12	1187	1151	14.19
01910	Grasse, FR (532.0 nm Nd:YAG laser)	1986/03/22 - 2005/07/30	8312	8110	3.22
01910	Grasse, FR (532.0 nm MeO laser)	2009/11/11 - 2017/02/07	1898	1831	1.42
01910	Grasse, FR (1064.0 nm Nd:YAG laser)	1989/09/23 - 1992/02/08	13	13	2.27
01910	Grasse, FR (1064.2 nm MeO laser)	2015/03/11 - 2017/02/19	1707	1673	1.43
56610	Haleakala, HI, USA	1984/11/13 - 1990/08/30	770	728	4.96
07941	Matera, IT	2003/02/22 - 2015/06/25	113	64	2.63
71110	McDonald, TX, USA	1969/08/20 - 1985/06/30	3604	3392	18.96
71111	MLRS1, TX, USA	1983/08/02 - 1988/01/27	631	513	20.44
71112	MLRS2, TX, USA	1988/02/29 - 2015/03/25	3670	3108	3.52
TOTAL		1969/08/20 - 2017/02/19	24545		

$$N_{CMB} = k_v(\omega_c - \omega_m) + (C_c - A_c)(\hat{z}_m \cdot \omega_c)(\hat{z}_m \times \omega_c) \quad (2e)$$

where k_v is the coefficient of viscous friction at the CMB and \hat{z}_m is a unit vector aligned with the polar axis of the mantle frame. The second part on the right-hand side of Eqn. (2e) is the inertial torque on an axis-symmetric fluid core.

2.3 Reduction model

The reduction model for the LLR data analysis has been implemented within a precise orbit determination and geodetic software: GINS ([33]) maintained by space geodesy teams at GRGS/OCA/CNES and written in Fortran90. The subroutines for the LLR data reduction within GINS is vetted through a step-wise comparison study conducted among the LLR analysis teams in OCA-Nice (this study), IMCCE-Paris and IfE-Hannover, by using simulated LLR data and DE421 as the planetary and lunar ephemeris. The modeling follows the recommendations of IERS 2010 ([29]). To avoid any systematics in the reduction model, the upper-limit on the discrepancy between the teams was fixed to 1 mm in one-way light time.

From each normal point, the emission time (in UTC) and the round trip time (in seconds) are used to iteratively solve for the reflection time in the light-time equations. A detailed description is available in Section 8 and Section 11 of [20] for a precise round-trip light-time computation.

A detailed description of the reduction model used for this study is provided in [15].

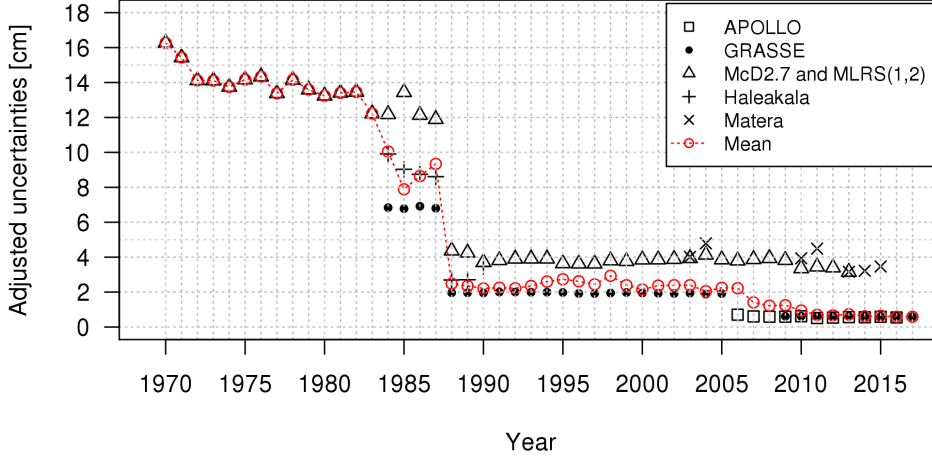


Figure 8: Annual mean of weights from different LLR stations after adjustments to uncertainties present within LLR observation (converted to 1-way LT [cm]).

2.4 Fitting procedure

2.4.1 Linearity and convergence

The WLS regression equation is represented by the linear relation in the following matrix form:

$$\hat{\beta}_{j,n} = (A_{ij}^T W_{ii} A_{ij})^{-1} A_{ij}^T W_{ii} X_{i,n-1} \quad (3)$$

where partial derivatives (A_{ij}) with respect to each parameter p_j are approximated by using numerical central differencing of the computed one-way light-time ($C(p_j)$). The choice of the magnitude of the parameter (δp_j) for the computation of A_{ij} is such that a linear region of the function $C(p_j)$ is explored. $\hat{\beta}_{j,n}$ gives the value of the estimated correction to be added to p_j for the n^{th} iteration and $X_{i,n-1}$ are the post-fit residuals ($O - C(p_j)$) from the $n - 1^{\text{th}}$ iteration. The WLS procedure is iterated until the χ^2 reaches a minimum value, after which numerical noise dominates.

2.4.2 Weighting and filtering scheme

The diagonal elements of the weighting matrix (W_{ii}) are the squares of the inverse of the inherent uncertainties (σ_i) of each observational computed using the normal point algorithm. Since the uncertainties are partly tied with the rejection scheme used in the normal point computation employed at each station, adjustments are required in cases where a lack of clean evolution of the uncertainties is noticed.

For APOLLO station observations, scaling the uncertainties of the normal points depending on the change of equipments, or a change in the normal point computation algorithm, is advised (see http://physics.ucsd.edu/~tmurphy/apollo/151201_notes.txt). Unrealistic uncertainties present in observations from Grasse, McDonald MLRS2 and Matera between time periods 1998-1999, 1996 and 2010-2012 respectively, are rescaled. Annual mean adjusted weights are given in Fig. (8). A sudden dip in the mean weights in 1987 is due to the change of laser (Ruby to Nd:YAG) at Grasse. Mean weights between 2005 to 2010 reach a minimum due to the operation of APOLLO station in the absence of observations from Grasse during the same period. Due to these necessary adjustments, a smooth evolution on the annual mean rms of the post-fit residuals is noticed.

A filtering scheme is enforced during the iterative fit of the parameters. At each iteration, before the estimation of $\hat{\beta}_{j,n}$, the residuals are passed through a $3\text{-}\sigma$ filter (σ recomputed at each iteration).

2.5 Biases

Changes in the ground station introduces biases in the residuals. These biases correspond either with a known technical development at the station (new equipment, change of optical fiber cables) or systematics. Any estimated bias can be correlated with a corresponding change in the ground station, provided the incidents have been logged. A list of known and detected biases have been included in Table 10.

2.6 Results

Table 7 gives the list of the adjusted parameters related to the Moon interior. Tables 8 and 9 give the fitted coordinates of the Moon reflectors and of the LLR stations. As the LLR observations are not included in the construction of the ITRF ([1]), small corrections to the LLR station coordinates help for the improvement of LLR residuals during the construction of the lunar ephemerides. The EOP parameters and the modeling of the Earth rotation are however kept fixed to the IERS convention (see section 2.3).

The solution INPOP_G with an axisymmetric core fitted to LLR observations serves as a validation of our lunar model and analysis procedure, against the DE430 JPL planetary and lunar ephemeris analysis described in [9] and EPM IAA RAS ephemeris in [26]. Only 532 nm wavelength LLR data are used for matching with the DE430 and EPM ephemeris. In [9], [26] and INPOP_G , gravity field coefficients up-to degree and order 6 are used for the Moon (GL0660b ([11])) and the Earth (GGM05C ([30])). Coefficients C_{32} , S_{32} and C_{33} are then included in the fit parameters as they improve the overall post-fit residuals. For INPOP_G , the improvement of the formal uncertainty compared to [26], especially in the estimation of parameter k_v/C_T indicates a strong dissipation mechanism within the Moon, through viscous torques at the fluid core-mantle boundary.

Differences between GL0660b values and fitted C_{32} , S_{32} and C_{33} from [9], [26] or in INPOP_G , are several orders of magnitude greater than the mean GRAIL uncertainties (see [11]). These results suggest that some significant effects impacting the LLR observations, are absorbed by the adjustment of the degree-3 of the full Moon gravity field.

The solution INPOP_{G+IR} refers to the addition of two years of IR LLR observations ([4]) following the same specification as of INPOP_G . This new dataset is constituted by 1707 normal points (7% of the total LLR data till date) from 2 years of operation in IR (1064 nm) wavelength at the ILRS station in Grasse¹. A review of the technical developments, accuracy and the homogeneity in the distribution (both spatial and temporal) of this new dataset can be found in [4]. This dataset is weighted at the same level as the APOLLO station normal points within the estimation procedure (see Appendix 2.4).

The first outcome from the introduction of the IR data sets is the improvement of the postfit residuals obtained for L1 reflector as one can see on Table 5. This is of course induced by the increase of normal points obtained for this reflector as discussed in 2.1.2.

The second conclusion is that because of only two years of data, the improvement brought by the addition of IR data on the estimated parameters characterizing the Moon and its inner structure is not massive (see Table 7).

¹The new IR LLR data from Grasse is made publicly available on <http://www.geoazur.fr/astrogeo/?href=observations/donnees/luneRG/brutes>

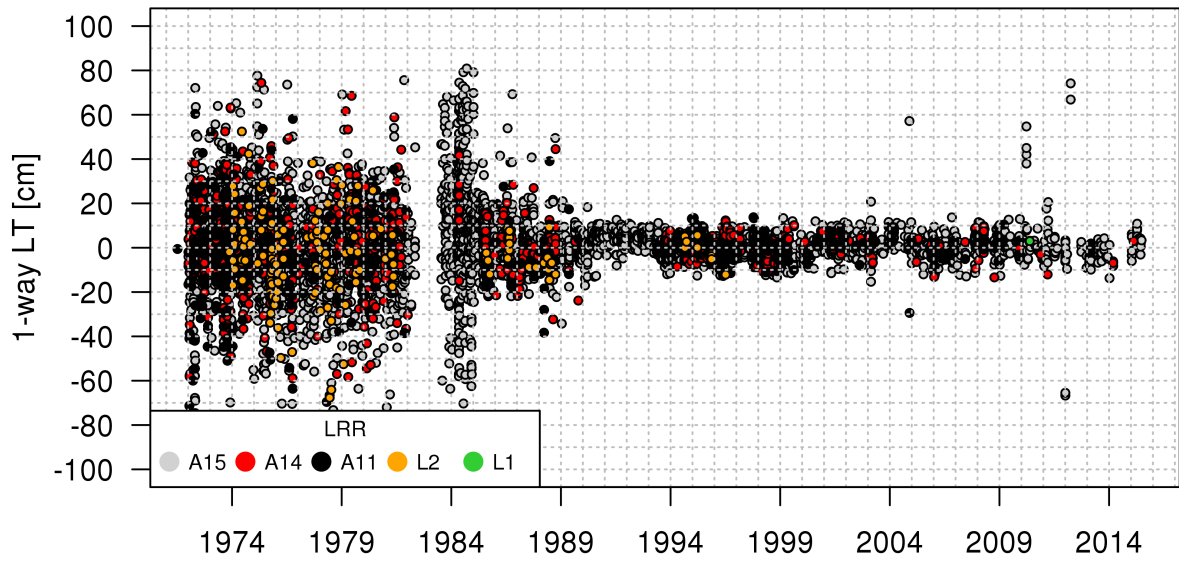


Figure 9: Post-fit residuals in (cm) vs time (year) obtained with INPOP17a specification for McDonal, MLRS1, MLRS2, Haleakala and Matera stations

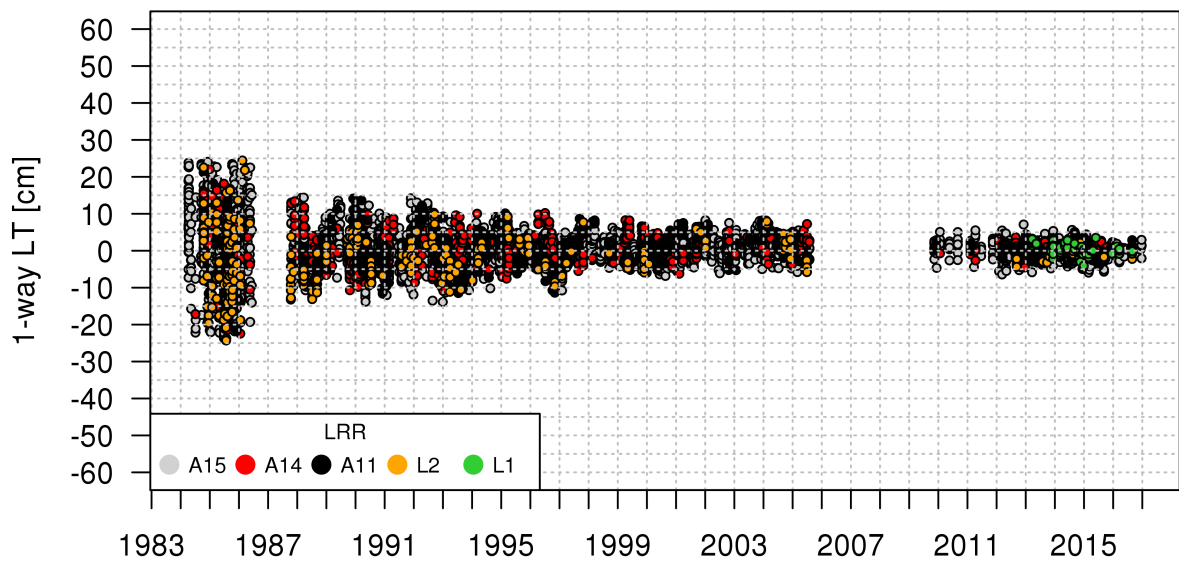


Figure 10: Post-fit residuals in (cm) vs time (year) obtained with INPOP17a specification for GRASSE station with the Green wavelength

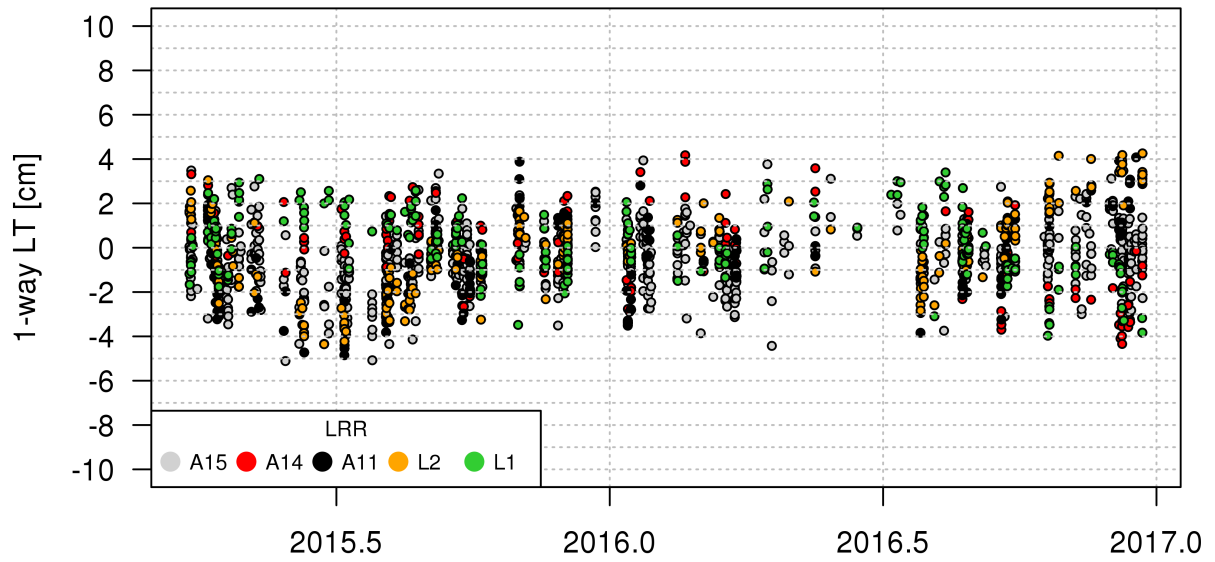


Figure 11: Post-fit residuals in (cm) vs time (year) obtained with INPOP17a specification for GRASSE station with the IR wavelenth

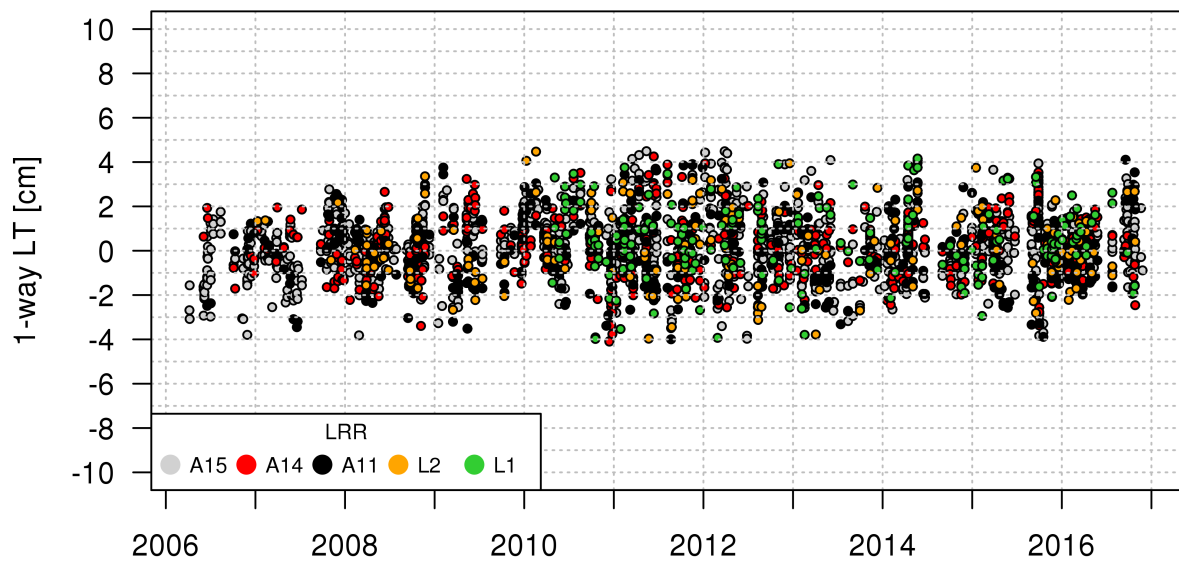


Figure 12: Post-fit residuals in (cm) vs time (year) obtained with INPOP17a specification for APOLLO station

Table 5: Reflector-wise statistics computed using residuals obtained with INPOP_G and INPOP_{G+IR} , within the fit intervals 01/01/2015 to 01/01/2017 (with a $3\text{-}\sigma$ filter), with the WRMS in m (RMS weighted by number of observation from each reflector).

LRRR	Grasse				APOLLO			
	INPOP_G	INPOP_{G+IR}	% change	NPTs	INPOP_G	INPOP_{G+IR}	% change	NPTs
A15	0.0183	0.0181	1.1	1018	0.0127	0.0127	0.2	344
A14	0.0203	0.0177	12.8	172	0.0192	0.0177	7.8	176
A11	0.0267	0.0239	10.5	215	0.0185	0.0169	8.7	164
L1	0.0215	0.0166	22.8	265	0.0186	0.0157	15.6	89
L2	0.0246	0.0215	12.6	256	0.0136	0.0137	-0.7	64
WRMS	0.0207	0.0189	TOTAL:	1926	0.0159	0.0149	TOTAL:	837

Table 6: Fixed parameters for the Earth-Moon system.

Parameter	Units	INPOP	DE430	EPM
$(EMRAT^\dagger - 81.300570) \times 10^6$		1.87	-0.92	-0.92
$(R_E - 6378.1366) \times 10^4$	km	0.0	-3	0.0
$(\dot{J}_{2E} - 2.6 \times 10^{-11})$	year ⁻¹	0.0	0.0	0.0
$(k_{20,E} - 0.335)$		0.0	0.0	0.0
$(k_{21,E} - 0.32)$		0.0	0.0	0.0
$(k_{22,E} - 0.30102)$		-0.01902	0.01898	-0.01902
$(\tau_{00,E} - 7.8 \times 10^{-2}) \times 10^2$	day	0.0	-1.4	0.0
$(\tau_{01,E} + 4.4 \times 10^{-2})$	day	0.0	0.0 [‡]	0.0
$\tau_{02,E} + 1.13 \times 10^{-1}) \times 10^1$	day	0.0	0.13	0.0
$(R_M - 1738.0)$	km	0.0	0.0	0.0
$(\alpha_C - 7.0 \times 10^{-4})$		0.0	0.0	0.0
$(k_{2,M} - 0.024059)$		0.0	0.0	0.0
$(l_2 - 0.0107)$		0.0	0.0	0.0

[†]: EMRAT is fit during the joint analysis between the lunar and planetary part.

[‡]: $\tau_{01,E}$ in [9] given as -0.0044 is a typographical error.

Table 7: Extended body parameters for the Earth and the Moon. Uncertainties for INPOP_G and INPOP_{G+IR} ($1-\sigma$) are obtained from a 5% jackknife (JK), while other solutions (DE430 and EPM) are assumed as ($1-\sigma$) formal uncertainties. † : C_{32} , S_{32} and C_{33} are reference values from the GRAIL analysis by [11]. ‡ : h_2 reference value from LRO-LOLA analysis by [17]. * : derived quantity

Parameter	Units	INPOP_G	INPOP_{G+IR}	DE430	EPM
$(GM_{EMB} - 8.997011400 \times 10^{-10}) \times 10^{19}$	AU ³ /day ²	4 ± 2	4 ± 2	-10	10 ± 5
$(\tau_{R1,E} - 7.3 \times 10^{-3}) \times 10^5$	day	0 ± 4	6 ± 3	6 ± 30	57 ± 5
$(\tau_{R2,E} - 2.8 \times 10^{-3}) \times 10^5$	day	9.2 ± 0.4	8.7 ± 0.3	-27 ± 2	5.5 ± 0.4
$(C_T/(m_M R^2) - 0.393140) \times 10^6$		6.9 ± 0.2	8.2 ± 0.2	2*	2*
$(C_{32} - 4.8404981 \times 10^{-6\dagger}) \times 10^9$		4.1 ± 0.3	3.9 ± 0.3	4.4	4.4 ± 0.1
$(S_{32} - 1.6661414 \times 10^{-6\dagger}) \times 10^8$		1.707 ± 0.006	1.666 ± 0.006	1.84	1.84 ± 0.02
$(C_{33} - 1.7116596 \times 10^{-6\dagger}) \times 10^8$		-1.19 ± 0.04	-2.40 ± 0.04	-3.6	-4.2 ± 0.2
$(\tau_M - 9 \times 10^{-2}) \times 10^4$	day	-14 ± 5	-35 ± 3	58.0 ± 100	60 ± 10
$(\frac{k_v}{C_T} - 1.6 \times 10^{-8}) \times 10^{10}$	day ⁻¹	12.7 ± 0.4	15.3 ± 0.5	4.0 ± 10.0	3.0 ± 2.0
$(f_c - 2.1 \times 10^{-4}) \times 10^6$		37 ± 3	42 ± 3	36 ± 28	37 ± 4
$(h_2 - 3.71 \times 10^{-2\dagger}) \times 10^3$		6.3 ± 0.2	6.8 ± 0.2	11.0 ± 6	6 ± 1
$Q_{27,212} - 45$ (derived)		3.9 ± 0.5	5.0 ± 0.2	0 ± 5	0 ± 1

Table 8: Fitted values of LLR station coordinates and velocities (expressed in meters and meters per year respectively), at J2000, for different solutions. The reference values correspond to ITRF2005. * indicates fixed parameters.

Station	Coordinate [m]	INPOP _G	INPOP _{G+IR}
Apache Point	x + 1463998.7870	-0.1269 ± 0.0004	-0.1285 ± 0.0004
	y + 5166632.8080	+0.0420 ± 0.0004	+0.0390 ± 0.0004
	z - 3435012.8560	-0.0119 ± 0.0014	+0.0099 ± 0.0014
	\dot{x} + 0.0141	+0.0009 ± 0.0001	+0.0011 ± 0.0001
	\dot{y} + 0.0015	+0.0012 ± 0.0001	+0.0016 ± 0.0001
	\dot{z} + 0.0064	+0.0084 ± 0.0016	+0.0064 ± 0.0016
Grasse	x - 4581692.1420	+0.0014 ± 0.0001	-0.0071 ± 0.0001
	y - 556196.0800	-0.0006 ± 0.0001	-0.0020 ± 0.0001
	z - 4389355.1080	-0.0039 ± 0.0012	-0.0040 ± 0.0012
	\dot{x} + 0.0156	+0.0018 ± 0.0001	+0.0024 ± 0.0001
	\dot{y} - 0.0184	+0.0006 ± 0.0012	+0.0007 ± 0.0012
	\dot{z} - 0.0089	+0.0048 ± 0.0002	+0.0044 ± 0.0001
Haleakala	x + 5466006.6900	+2.9163 ± 0.0019	+2.9168 ± 0.0019
	y + 2404427.2460	+1.2864 ± 0.0031	+1.2882 ± 0.0031
	z - 2242187.8750	+9.9607 ± 0.0078	+9.9610 ± 0.0078
	\dot{x} + 0.0122 *	-	-
	\dot{y} - 0.0622 *	-	-
	\dot{z} - 0.0310 *	-	-
Matera	x - 4641978.8100 *	-	-
	y - 1393067.5310 *	-	-
	z - 4133249.4800 *	-	-
	\dot{x} + 0.0180 *	-	-
	\dot{y} - 0.0192 *	-	-
	\dot{z} - 0.0140 *	-	-
McDonald	x + 1330781.4610	-0.0120 ± 0.0142	-0.0146 ± 0.0142
	y + 5328755.4550	-0.6717 ± 0.0037	-0.6682 ± 0.0037
	z - 3235697.5110	+0.6911 ± 0.0315	+0.6446 ± 0.0315
	\dot{x} + 0.0124	-0.0040 ± 0.0006	-0.0041 ± 0.0006
	\dot{y} - 0.0009	-0.0177 ± 0.0002	-0.0176 ± 0.0002
	\dot{z} + 0.0053	+0.0343 ± 0.0014	+0.0325 ± 0.0014
MLRS1	x + 1330121.1440	+0.0920 ± 0.0234	+0.0875 ± 0.0234
	y + 5328532.2620	+0.0440 ± 0.0204	+0.0369 ± 0.0204
	z - 3236146.6030	-0.4753 ± 0.0213	-0.4798 ± 0.0213
	\dot{x} + 0.0124 *	-	-
	\dot{y} - 0.0009 *	-	-
	\dot{z} + 0.0053 *	-	-
MLRS2	x + 1330021.1090	-0.0119 ± 0.0008	-0.0118 ± 0.0008
	y + 5328401.8580	-0.0171 ± 0.0003	-0.0148 ± 0.0003
	z - 3236480.7680	-0.0098 ± 0.0018	-0.0129 ± 0.0018
	\dot{x} + 0.0124	+0.0004 ± 0.0004	+0.0005 ± 0.0004
	\dot{y} - 0.0009	+0.0014 ± 0.0001	+0.0015 ± 0.0001
	\dot{z} + 0.0053	+0.0003 ± 0.0007	+0.0007 ± 0.0007

Table 9: Fitted values of selenocentric coordinates of reflectors (in meters). The reference values are from a previous release of INPOP (version 13c).

Reflector	Coordinate [m]	INPOP_G	INPOP_{G+IR}
Apollo 11	x - 1591924.5110	+42.2267 ± 0.0181	+42.1831 ± 0.0181
	y - 690802.5820	-103.0306 ± 0.0052	-102.9494 ± 0.0052
	z - 21003.7740	-0.1029 ± 0.0118	-0.1035 ± 0.0118
Apollo 14	x - 1652725.8400	-36.1039 ± 0.0196	-36.0924 ± 0.0196
	y + 520890.3070	-107.1523 ± 0.0140	-107.0555 ± 0.0140
	z + 109730.4800	-0.1173 ± 0.0028	-0.1287 ± 0.0028
Apollo 15	x - 1554674.5700	+3.8976 ± 0.0155	+3.8898 ± 0.0155
	y - 98196.2940	-100.6368 ± 0.0068	-100.5489 ± 0.0068
	z - 765005.6960	-0.5951 ± 0.0067	-0.6184 ± 0.0067
Lunakhod 1	x + 1330021.1090	-53.0291 ± 0.0149	-52.9913 ± 0.0149
	y + 5328401.8580	-71.7348 ± 0.0042	-71.6464 ± 0.0042
	z - 3236480.7680	-0.8370 ± 0.0021	-0.8250 ± 0.0021
Lunakhod 2	x - 1114345.4960	+49.3650 ± 0.0145	+49.3269 ± 0.0145
	y + 781226.5970	-86.7535 ± 0.0015	-86.6622 ± 0.0015
	z - 1076059.3350	-0.6976 ± 0.0083	-0.6982 ± 0.0083

Table 10: Estimated values of station biases over different periods (2-way light time in cm)

Bias #	Station	Date	Bias 2-way light time [cm]	
			INPOP _G	INPOP _{G+IR}
1	Apache Point	2006/04/07 - 2010/11/01	0.24 ± 0.01	-0.24 ± 0.01
2		2007/12/15 - 2008/06/30	-3.86 ± 0.04	-3.90 ± 0.04
3		2008/09/20 - 2009/06/20	2.83 ± 0.07	2.83 ± 0.07
4		2010/11/01 - 2012/04/07	-5.74 ± 0.04	-5.98 ± 0.04
5		2012/04/07 - 2013/09/02	9.18 ± 0.01	9.12 ± 0.01
6	Grasse	1984/06/01 - 1986/06/13	-8.76 ± 0.45	-6.49 ± 0.45
7		1987/10/01 - 2005/08/01	1.32 ± 0.07	2.47 ± 0.07
8		1993/03/01 - 1996/10/01	10.32 ± 0.02	10.38 ± 0.02
9		1996/12/10 - 1997/01/18	17.33 ± 0.06	16.92 ± 0.06
10		1997/02/08 - 1998/06/24	19.49 ± 0.01	19.56 ± 0.01
11		2004/12/04 - 2004/12/07	-5.74 ± 0.31	-7.07 ± 0.31
12		2005/01/03 - 2005/01/06	-5.39 ± 0.01	-6.72 ± 0.01
13		2009/11/01 - 2014/01/01	0.59 ± 0.08	0.34 ± 0.08
14		2015/12/20 - 2015/12/21	-	-88.34 ± 0.03
15		2016/06/01 - 2018/01/01	2.52 ± 0.01	2.46 ± 0.01
16	Haleakala	1984/11/01 - 1990/09/01	2.36 ± 0.29	2.55 ± 0.29
17		1984/11/01 - 1986/04/01	-3.76 ± 0.56	-3.61 ± 0.56
18		1986/04/02 - 1987/07/30	13.60 ± 0.02	13.07 ± 0.02
19		1987/07/31 - 1987/08/14	1.92 ± 0.64	1.83 ± 0.64
20		1985/06/09 - 1985/06/10	-12.25 ± 0.09	-13.18 ± 0.09
21		1987/11/10 - 1988/02/18	20.42 ± 0.42	19.49 ± 0.42
22		1990/02/06 - 1990/09/01	15.26 ± 0.11	14.32 ± 0.11
23	Matera	2003/01/01 - 2016/01/01	0.73 ± 7.24	4.62 ± 7.24
24	McDonald	1969/01/01 - 1985/07/01	-37.98 ± 1.20	-37.88 ± 1.20
25		1971/12/01 - 1972/12/05	28.71 ± 0.88	28.21 ± 0.88
26		1972/04/21 - 1972/04/27	88.17 ± 0.71	88.09 ± 0.71
27		1974/08/18 - 1974/10/16	-112.58 ± 0.37	-112.08 ± 0.37
28		1975/10/05 - 1976/03/01	30.48 ± 0.22	28.44 ± 0.22
29		1983/12/01 - 1984/01/17	10.49 ± 1.69	11.06 ± 1.69
30		1969/01/01 - 1971/12/31	2249.64 ± 0.83	2249.19 ± 0.83
31		MLRS1	1983/08/01 - 1988/01/28	39.99 ± 2.01

Table 11: Statistics of the residuals obtained after the INPOP13c fit for common data sample between INPOP13c and INPOP10e. For comparison, means and standard deviations of residuals obtained with INPOP10e.

Type of data		Nbr	Time Interval	INPOP17a		INPOP13c	
Mercury	range [m]	462	1971.29 - 1997.60	-167.975	1605.318	-101.524	861.494
Mercury Mariner	range [m]	2	1974.24 - 1976.21	-75.645	78.743	-196.405	19.636
Mercury flybys Mess	ra [mas]	3	2008.03 - 2009.74	0.868	1.329	0.901	1.355
Mercury flybys Mess	de [mas]	3	2008.03 - 2009.74	2.379	2.209	2.472	2.408
Mercury flybys Mess	range [m]	3	2008.03 - 2009.74	-1.593	1.840	3.190	7.699
Mercury Messenger	range [m]	269	2011.39 - 2013.20	1.250	8.603	4.008	12.387
Venus	VLBI [mas]	46	1990.70 - 2010.86	1.195	2.356	1.591	2.575
Venus	range [m]	489	1965.96 - 1990.07	497.493	2236.789	504.569	2237.636
Venus Vex	range [m]	24249	2006.32 - 2011.45	2.762	6.576	2.362	6.693
Mars	VLBI [mas]	194	1989.13 - 2013.86	0.124	0.348	0.116	0.333
Mars Mex	range [m]	29203	2005.17 - 2016.37	-0.059	3.552	4.669	23.361
Mars MGS	range [m]	2417	1999.33 - 2006.72	4.370	3.890	0.362	3.777
Mars Ody	range [m]	21673	2002.14 - 2014.00	2.155	5.797	2.47	7.200
Mars Path	range [m]	90	1997.51 - 1997.73	-0.233	13.268	19.324	14.096
Mars Vkg	range [m]	1257	1976.55 - 1982.87	-8.203	60.833	-1.494	41.189
Jupiter	VLBI [mas]	24	1996.54 - 1997.94	-0.702	11.376	-0.450	11.069
Jupiter	ra [arcsec]	6532	1914.54 - 2008.49	-0.005	0.308	-0.039	0.297
Jupiter	de [arcsec]	6394	1914.54 - 2008.49	-0.047	0.302	-0.048	0.301
Jupiter flybys	ra [mas]	5	1974.92 - 2001.00	2.396	2.351	2.554	2.961
Jupiter flybys	de [mas]	5	1974.92 - 2001.00	-9.148	9.895	-10.853	11.425
Jupiter flybys	range [m]	5	1974.92 - 2001.00	-644.521	1414.411	-985.957	1775.627
Saturne	ra [arcsec]	7971	1913.87 - 2008.34	0.023	0.304	-0.006	0.293
Saturne	de [arcsec]	7945	1913.87 - 2008.34	-0.012	0.266	-0.012	0.266
Saturne VLBI Cass	ra [mas]	10	2004.69 - 2009.31	0.172	0.553	0.113	0.630
Saturne VLBI Cass	de [mas]	10	2004.69 - 2009.31	-0.203	0.272	-0.115	0.331
Saturne Cassini	tracking range [m]	169	2004.41 : 2014.38	5.059	31.618	-471.270	340.340

Table 12: Statistics of the residuals obtained after the INPOP13c fit for common data sample between INPOP13c and INPOP10e. For comparison, means and standard deviations of residuals obtained with INPOP10e are given.

Type of data		Nbr	Time Interval	INPOP10e		INPOP13c	
Uranus	ra [arcsec]	13016	1914.52 - 2011.74	-0.003	0.216	0.007	0.205
Uranus	de [arcsec]	13008	1914.52 - 2011.74	-0.027	0.234	-0.006	0.234
Uranus flybys	ra [arcsec]	1	1986.07 - 1986.07	-0.021	0.000	-0.021	0.000
Uranus flybys	de [arcsec]	1	1986.07 - 1986.07	-0.064	0.000	-0.028	0.000
Uranus flybys	range [m]	1	1986.07 - 1986.07	-0.080	0.000	20.771	0.000
Neptune	ra [arcsec]	5395	1913.99 - 2007.88	0.008	0.259	0.003	0.258
Neptune	de [arcsec]	5375	1913.99 - 2007.88	-0.011	0.303	-0.002	0.299
Neptune flybys	ra [arcsec]	1	1989.65 - 1989.65	-0.015	0.000	-0.011	0.000
Neptune flybys	de [arcsec]	1	1989.65 - 1989.65	-0.023	0.000	-0.005	0.000
Neptune flybys	range [m]	1	1989.65 - 1989.65	-2.869	0.000	51.507	0.000
Pluto	ra [arcsec]	3053	1914.06 - 2008.49	-0.035	0.566	0.020	0.574
Pluto	de [arcsec]	3052	1914.06 - 2008.49	0.010	0.479	0.001	0.525
Pluto Occ	ra [arcsec]	13	2005.44 - 2009.64	-0.009	0.045	-0.100	0.044
Pluto Occ	de [arcsec]	13	2005.44 - 2009.64	0.008	0.026	0.000	0.027
Pluto HST	ra [arcsec]	5	1998.19 - 1998.20	-0.052	0.044	-0.018	0.044
Pluto HST	de [arcsec]	5	1998.19 - 1998.20	-0.001	0.048	-0.026	0.048

References

- [1] Z. Altamimi, P. Rebischung, L. Métivier, and X. Collilieux. ITRF2014: A new release of the International Terrestrial Reference Frame modeling nonlinear station motions. Journal of Geophysical Research (Solid Earth), 121:61096131, August 2016.
- [2] B. Carry. Asteroid masses. Private communication.
- [3] B. Carry. Asteroid masses. Planetary and Space science, 525:533–538, November 2012.
- [4] C Courde, J M Torre, E Samain, M Aimar, D Albanese, P Exertier, and D Feraudy. Lunar Laser Ranging in infrared at the Grasse laser station. 2016.
- [5] A Fienga, H Manche, J Laskar, M Gastineau, and A Verma. INPOP new release: INPOP13b. ArXiv e-prints, 423, 2014.
- [6] A Fienga, H Manche, J Laskar, M Gastineau, A Verma, Imcce-cnrs Umr, and Av Denfert-rochereau. DPAC INPOP final release : INPOP10e. 2012.
- [7] W. M. Folkner. DE436 planetary ephemerides spice delivery. <https://naif.jpl.nasa.gov/pub/naif/JUN0/kernels/spk/de436s.bsp.1bl>.
- [8] W. M. Folkner, J. G. Williams, D. H. Boggs, R. S. Park, and P. Kuchynka. The Planetary and Lunar Ephemerides DE430 and DE431. Interplanetary Network Progress Report, 196:C1, February 2014.
- [9] W. M. Folkner, J. G. Williams, D. H. Boggs, R. S. Park, and P. Kuchynka. The Planetary and Lunar Ephemerides DE430 and DE431. 2014.
- [10] H. S. Jeon, S. Cho, Y. S. Kwak, J. K. Chung, J. U. Park, D. K. Lee, and M. Kuzmich-Cieslak. Mass density of the upper atmosphere derived from Starlette’s Precise Orbit Determination with Satellite Laser Ranging. Ap&SS, 332:341–351, April 2011.
- [11] Alex S. Konopliv, Ryan S. Park, Dah Ning Yuan, Sami W. Asmar, Michael M. Watkins, James G. Williams, Eugene Fahnestock, Gerhard Kruizinga, Meegyeong Paik, Dmitry Strelakov, Nate Harvey, David E. Smith, and Maria T. Zuber. The JPL lunar gravity field to spherical harmonic degree 660 from the GRAIL Primary Mission. Journal of Geophysical Research E: Planets, 118(7):1415–1434, 2013.
- [12] P. Kuchynka, J. Laskar, A. Fienga, and H. Manche. A ring as a model of the main belt in planetary ephemerides. A&A, 514:A96+, May 2010.
- [13] D. M. Lucchesi, L. Anselmo, M. Bassan, C. Pardini, R. Peron, G. Pucacco, and M. Visco. Testing the gravitational interaction in the field of the Earth via satellite laser ranging and the Laser Ranged Satellites Experiment (LARASE). Classical and Quantum Gravity, 32(15):155012, August 2015.
- [14] Florent Lyard, Fabien Lefevre, Thierry Letellier, and Olivier Francis. Modelling the global ocean tides: modern insights from FES2004. Ocean Dynamics, 56(5-6):394–415, dec 2006.
- [15] H. Manche. Modele dynamique des ephemerides INPOP and ajustement aux donnes LLR. PhD thesis, Observatoire de Paris, 2011.

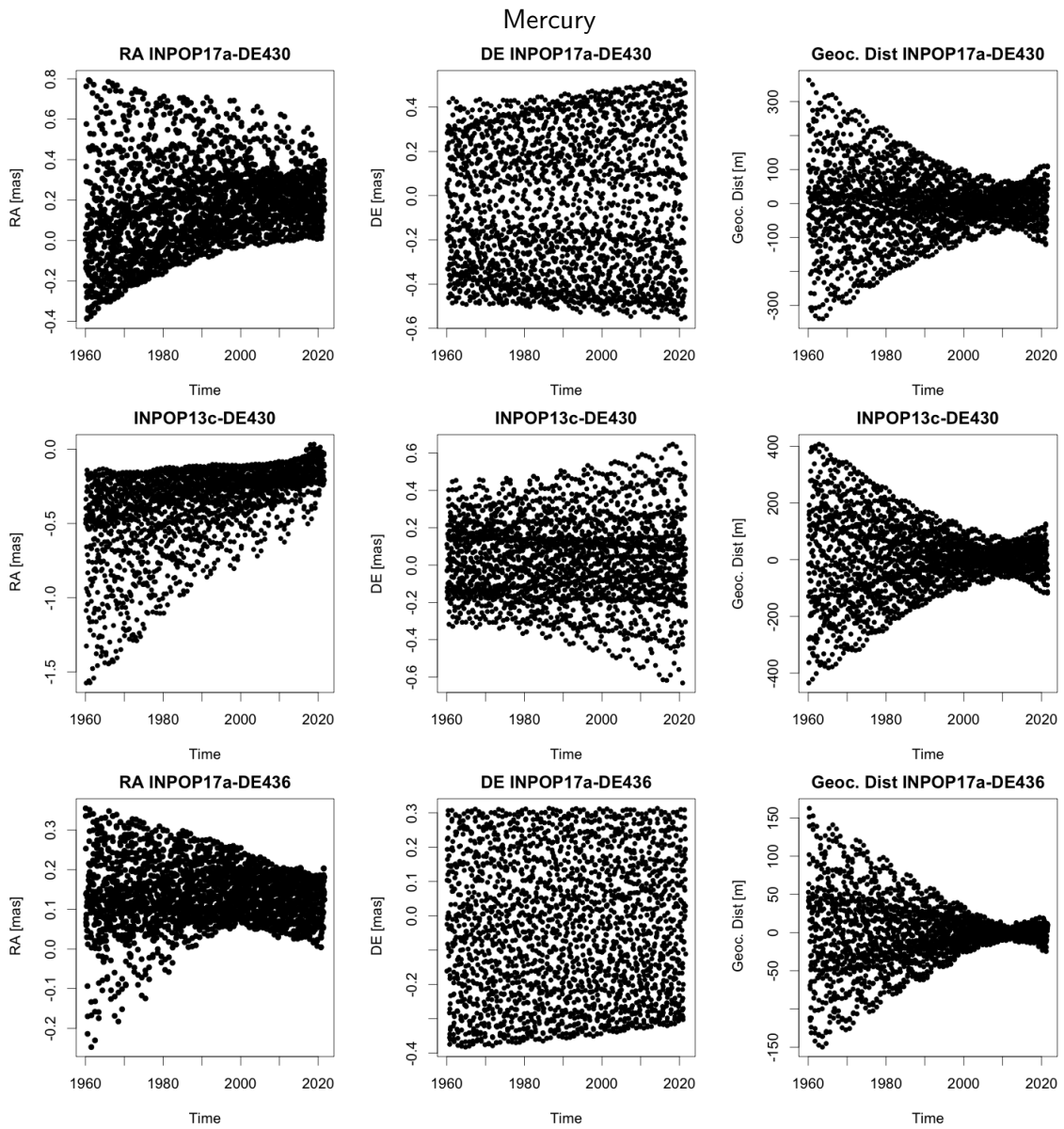


Figure 13: Differences in α, δ and geocentric distances between INPOP17a, INPOP13c, DE430 and DE436.

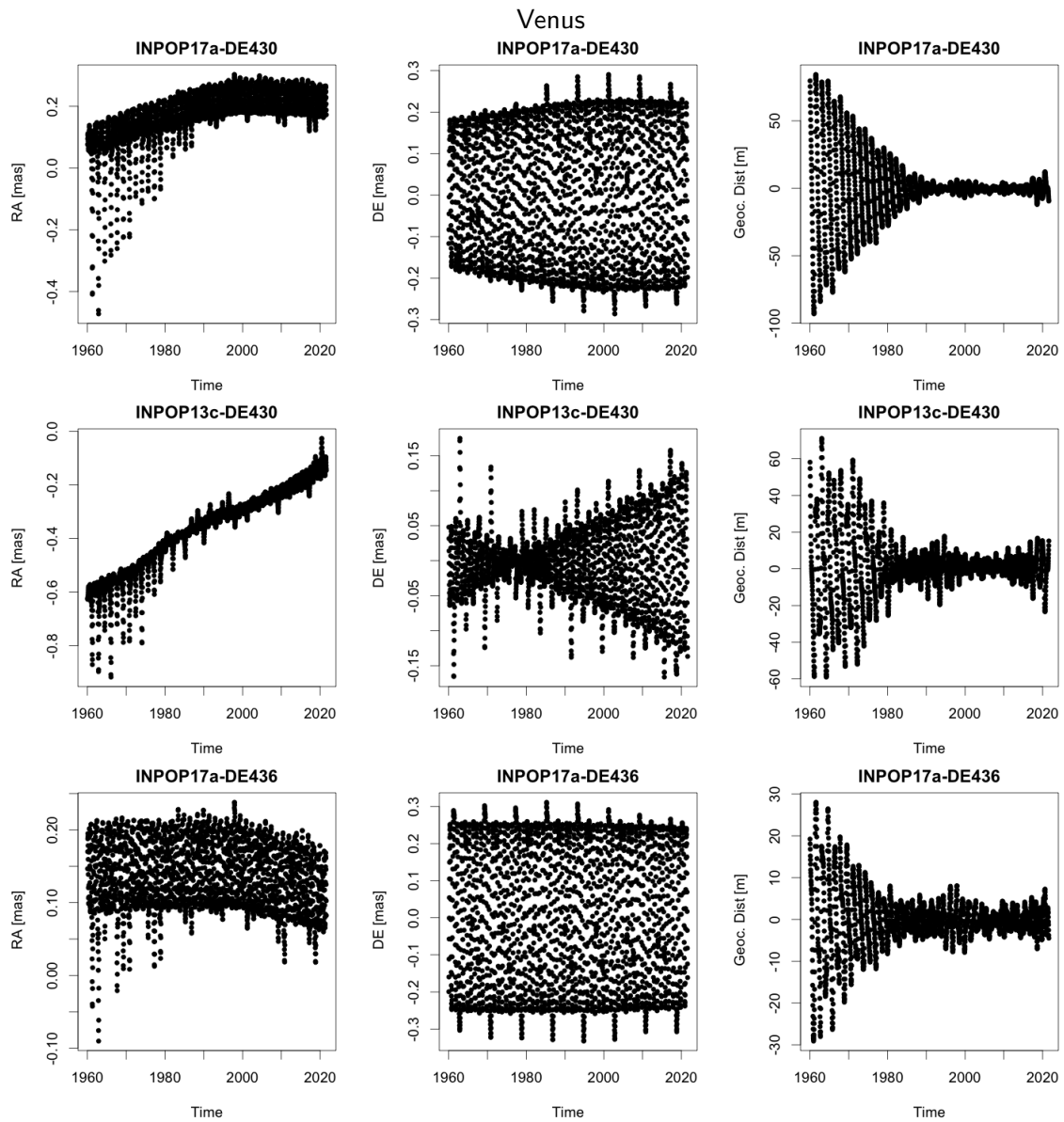


Figure 14: Differences in α , δ and geocentric distances between INPOP17a, INPOP13c, DE430 and DE436.

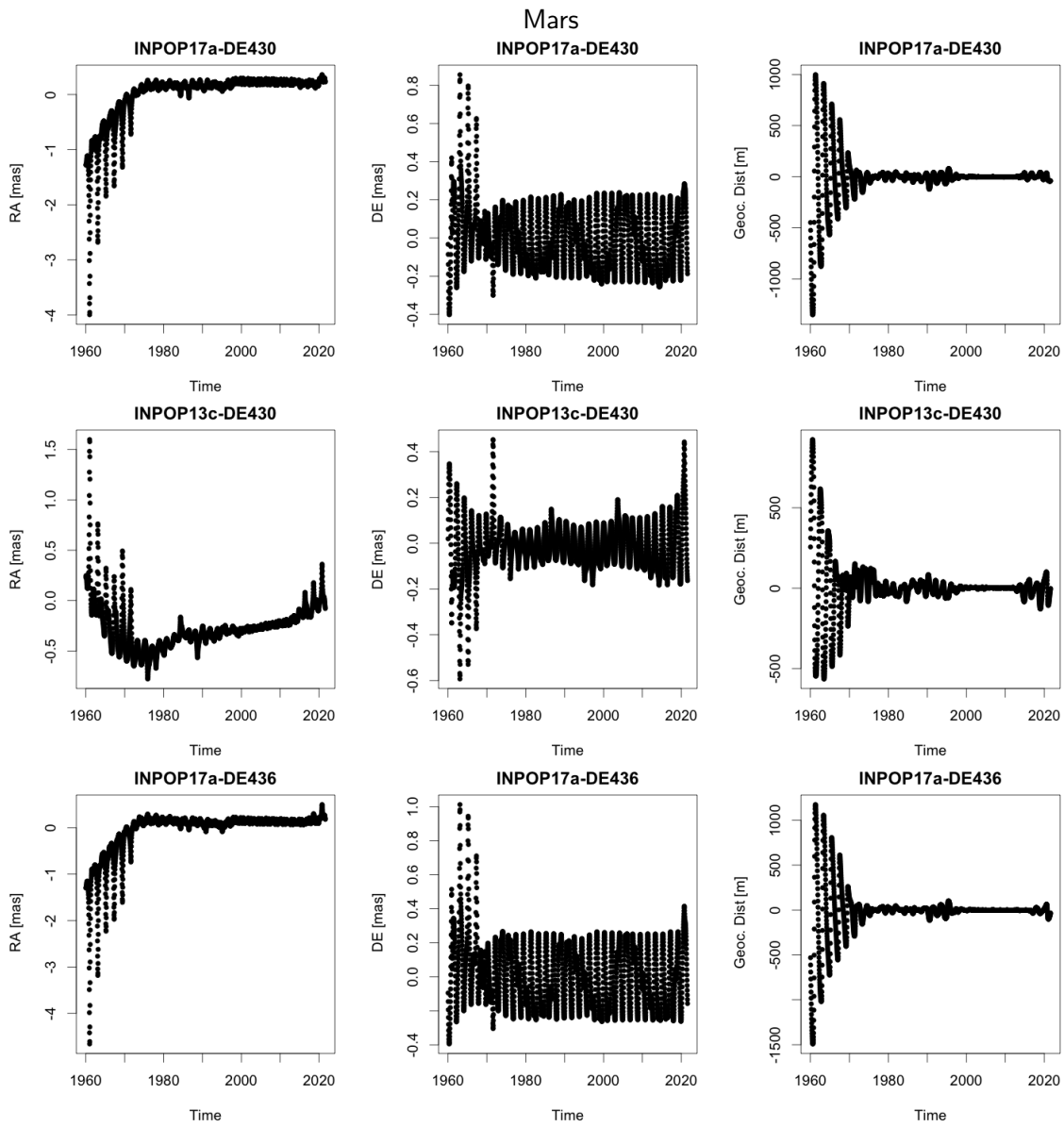


Figure 15: Differences in α, δ and geocentric distances between INPOP17a, INPOP13c, DE430 and DE436.

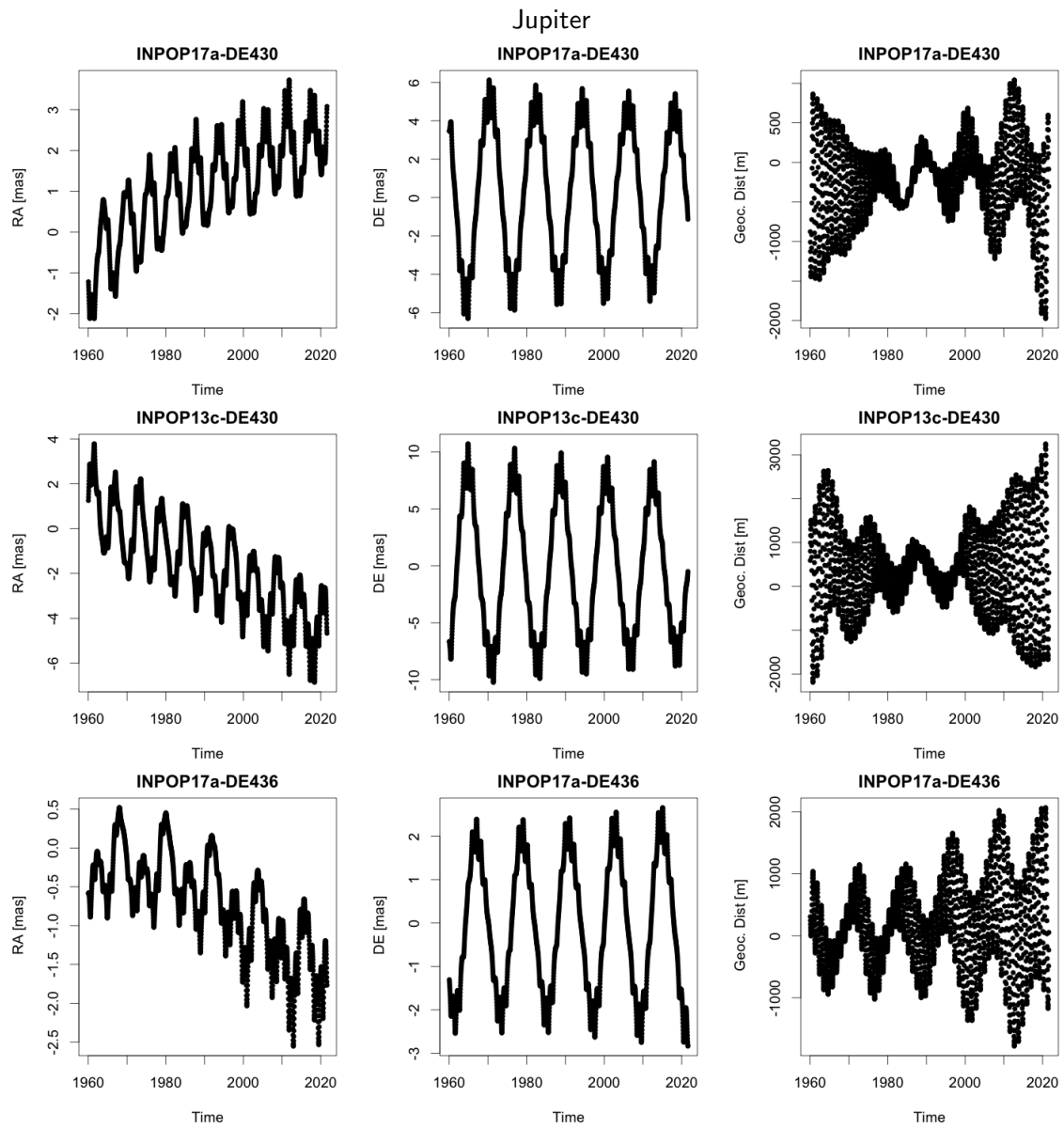


Figure 16: Differences in α , δ and geocentric distances between INPOP17a, INPOP13c, DE430 and DE436.

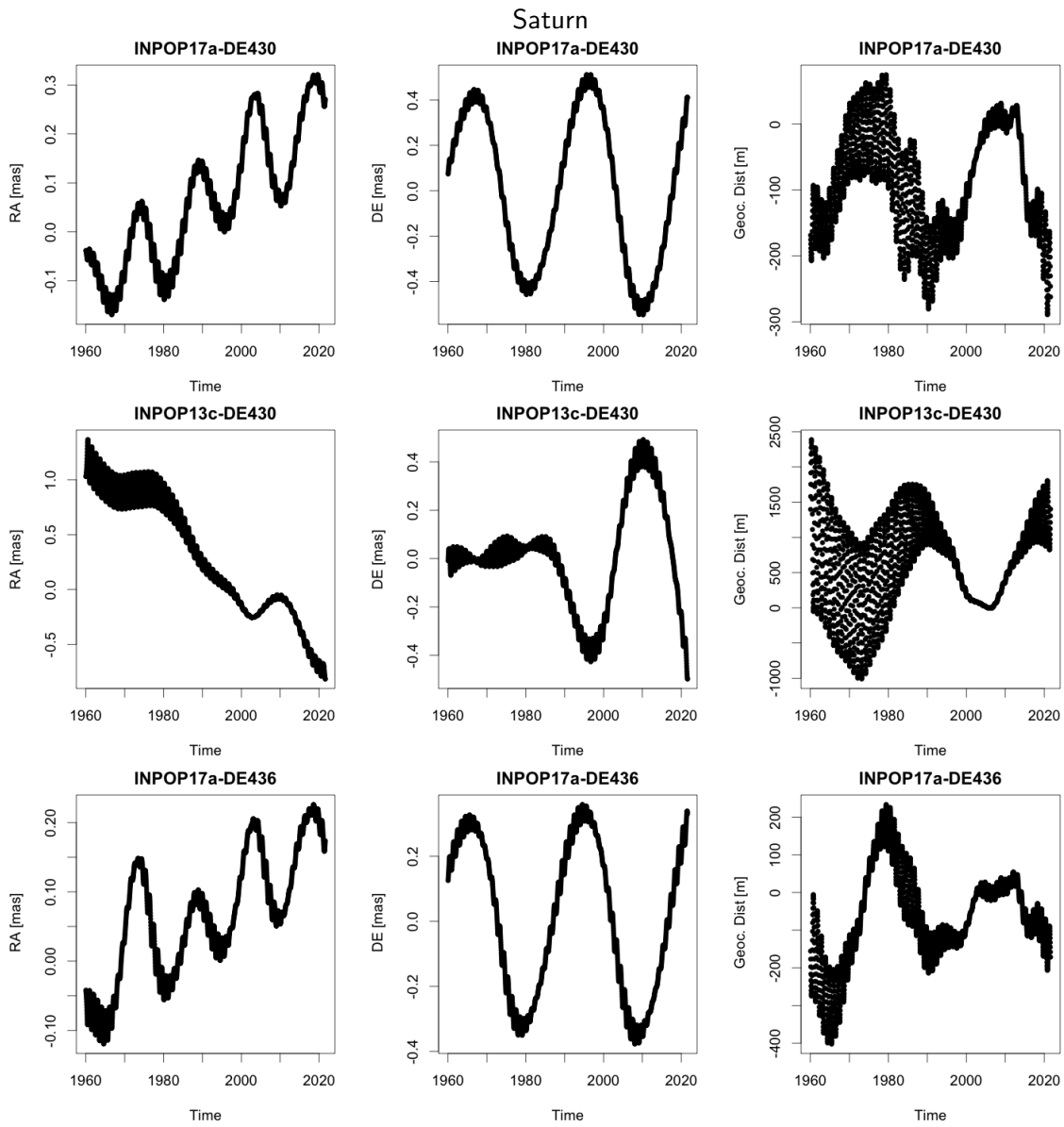


Figure 17: Differences in α, δ and geocentric distances between INPOP17a, INPOP13c, DE430 and DE436.

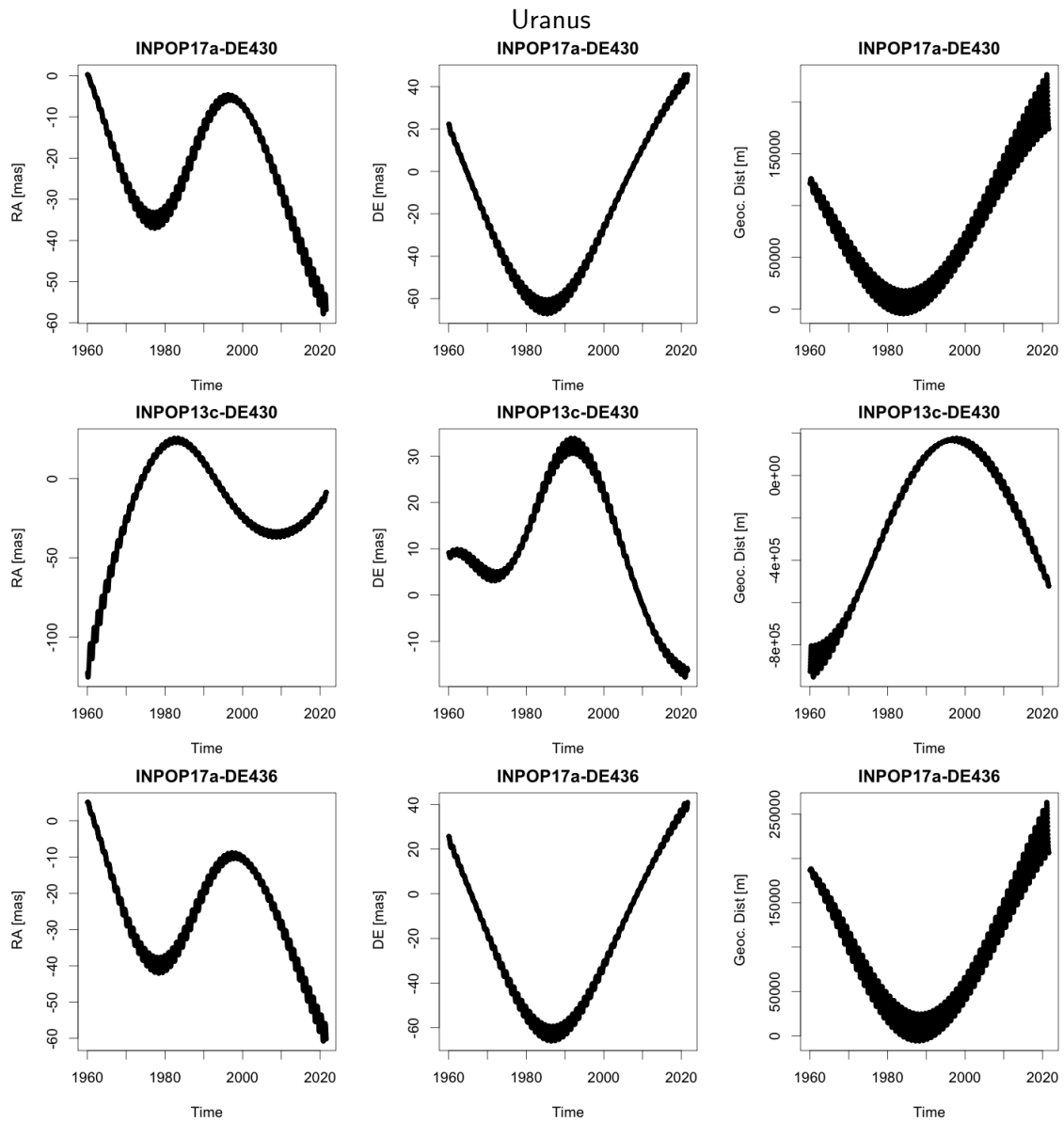


Figure 18: Differences in α , δ and geocentric distances between INPOP17a, INPOP13c, DE430 and DE436.

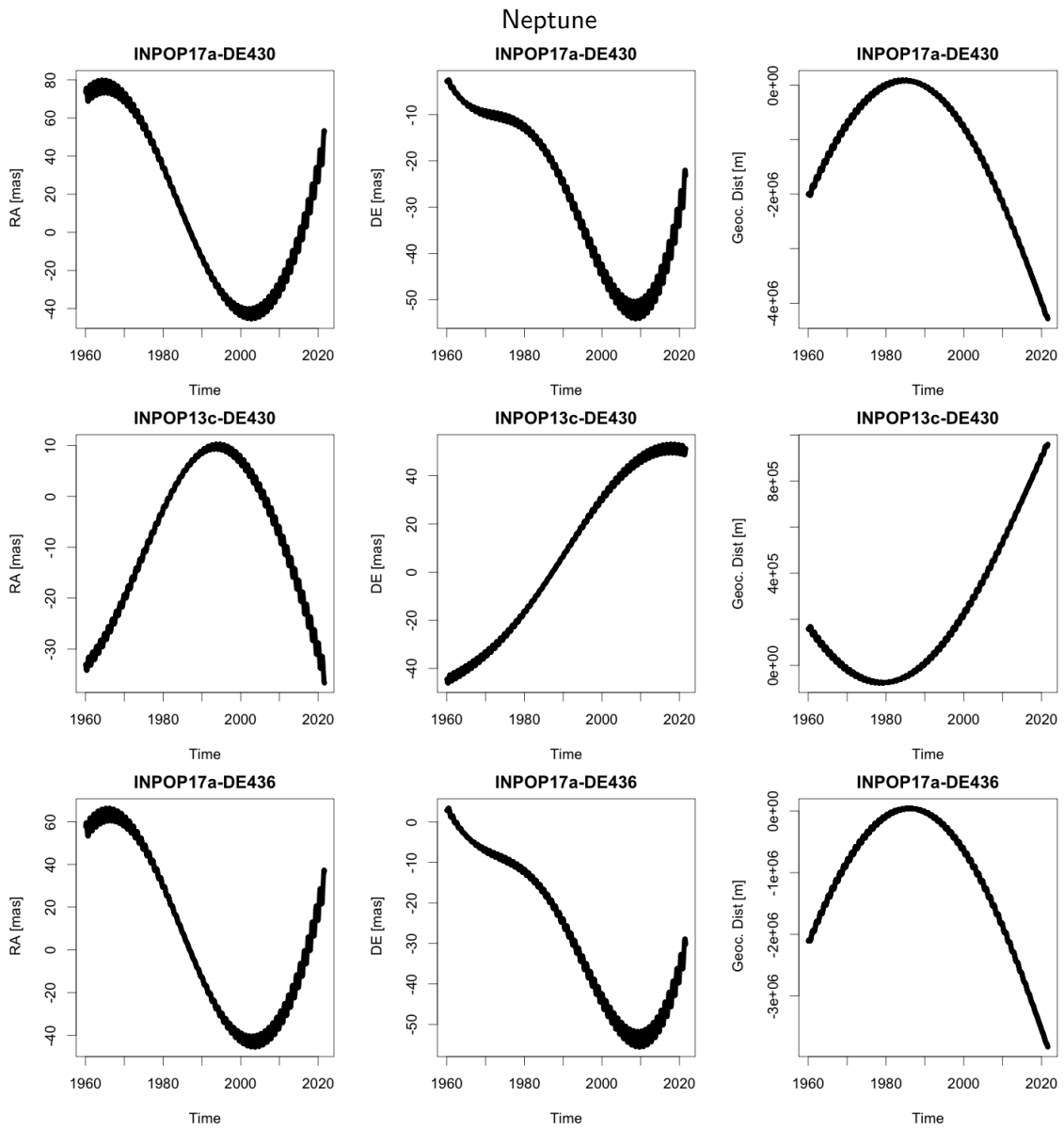


Figure 19: Differences in α, δ and geocentric distances between INPOP17a, INPOP13c, DE430 and DE436.

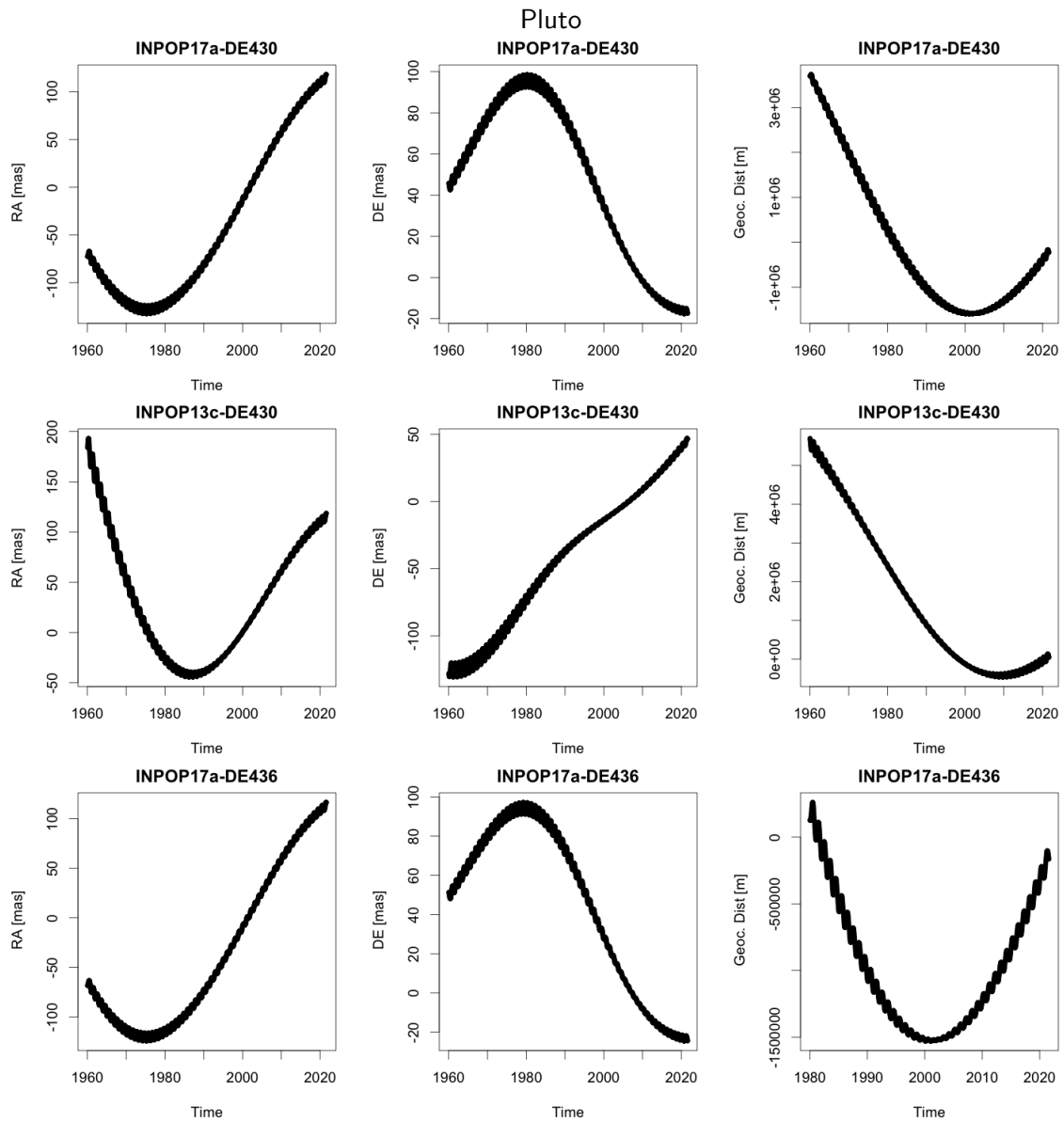


Figure 20: Differences in α , δ and geocentric distances between INPOP17a, INPOP13c, DE430 and DE436.

Table 13: Asteroid masses obtained with INPOP17a and compared with values extracted from [2] and [8]. Column 7 gives the value of this maximum impact of each asteroid on the Earth-Mars distances as defined in [12]. The star indicates the masses obtained with *a priori sigma* deduced from published estimations given by [2].

IAU designation	INPOP17a $\times 10^{-18}$ kg	1- σ $\times 10^{-18}$ kg	Carry 2012 $\times 10^{-18}$ kg	1- σ $\times 10^{-18}$ kg	DE430 $\times 10^{-18}$ kg	Impact km
4*	259.120	0.773	259.076	0.001	259.087	1198.953
1*	938.406	2.214	938.416	0.013	941.295	793.741
2*	204.566	1.466	204.000	3.160	208.658	146.270
324*	8.797	0.364	10.000	0.957	9.333	93.536
10*	86.670	4.291	84.200	3.360	83.061	77.003
19	10.268	0.561	8.910	0.770	6.961	59.069
3	25.301	0.788	26.800	2.440	24.314	55.639
704*	41.777	4.398	33.300	4.340	35.328	34.492
532*	17.776	1.207	12.600	2.530	6.261	32.714
9	16.306	0.731	7.050	1.870	7.244	29.606
7*	10.080	0.558	12.500	1.200	14.360	27.822
29	8.602	1.234	12.600	1.880	13.280	26.673
24	2.158	2.467	5.890	1.910	12.729	26.131
31	31.197	4.354	17.200	3.850	42.635	23.466
13	10.370	1.553	9.250	3.080	12.078	22.038
15*	29.557	1.052	31.100	1.580	31.444	21.555
6*	9.109	0.873	12.200	2.980	5.587	21.150
11*	6.986	1.011	5.890	0.516	8.950	17.301
139*	9.046	1.028	6.680	1.150	2.839	16.687
105	2.635	0.606	1.530	0.537	2.497	15.196
20	5.046	1.120	5.150	0.635	0.618	14.763
372	7.542	2.960	5.550	0.772	11.735	13.796
8*	4.230	0.347	6.560	1.110	3.962	12.664
45	0.269	0.049	NA	NA	5.663	11.790
405	3.134	0.462	1.680	0.518	3.748	11.378
18	5.630	0.394	4.240	1.010	1.350	11.287
354	5.804	1.393	7.180	2.570	10.654	10.253
511*	18.066	3.843	29.100	5.760	34.938	10.248
52	30.541	2.537	24.000	3.220	16.647	9.841
16	21.068	2.122	25.400	6.150	22.930	9.701
419	1.322	0.384	2.010	0.657	2.472	9.585
78	0.429	0.269	1.770	1.350	0.565	9.389
23	2.525	0.428	2.250	0.437	1.274	9.067
488	4.648	1.864	2.410	1.160	1.287	8.614
230	0.845	0.665	2.190	0.598	1.184	7.620
187	0.287	0.138	1.860	0.794	6.331	7.592
344	3.818	0.627	1.390	0.478	3.609	7.465

Table 14: Asteroid masses obtained with INPOP17a and compared with values extracted from [3], [2] and [8]. Column 7 gives the value of this maximum impact of each asteroid on the Earth-Mars distances as defined in [12]. The star indicates the masses obtained with *a priori sigma* deduced from published estimations given by [2].

IAU designation	INPOP17a $\times 10^{-18}$ kg	1- σ $\times 10^{-18}$ kg	Carry 2012 $\times 10^{-18}$ kg	1- σ $\times 10^{-18}$ kg	DE430 $\times 10^{-18}$ kg	Impact km
130	9.406	2.086	6.600	0.398	6.679	7.054
111	3.053	1.146	1.710	0.487	0.225	6.985
42	1.586	0.445	1.410	0.613	1.859	6.829
469	2.122	0.551	5.130	1.130	2.170	6.107
356	3.978	0.704	NA	NA	1.802	5.759
88	11.815	1.646	11.100	1.460	17.321	5.742
60	0.792	0.282	0.315	0.032	0.342	5.733
128	2.132	1.485	8.070	1.300	6.486	5.624
59	5.558	1.500	3.060	0.480	4.261	5.325
98	1.647	0.744	0.893	0.199	1.642	5.195
89	1.149	0.391	7.620	0.659	2.287	4.815
451	21.881	4.796	11.900	4.300	15.429	4.742
107	16.089	4.422	12.000	1.000	11.236	4.630
65*	20.036	5.633	13.700	3.420	21.378	4.536
21*	1.848	0.978	NA	NA	1.700	4.527
134	4.917	1.151	2.020	0.736	2.260	4.171
54	12.134	1.136	NA	NA	3.780	4.091
120	9.116	3.491	6.360	0.795	7.991	3.906
173	7.330	1.529	NA	NA	2.630	3.811
22	0.075	0.709	8.070	1.220	8.083	3.756
444	8.200	1.865	NA	NA	6.097	3.725
84	0.545	0.268	NA	NA	0.845	3.698
185	7.446	1.713	4.900	2.530	7.633	3.650
37	0.583	0.272	NA	NA	1.469	3.551
53	0.806	0.337	NA	NA	0.419	3.550
410	5.331	0.861	NA	NA	2.432	3.388
85	5.070	1.155	2.800	1.130	6.220	3.375
129	6.246	1.556	NA	NA	3.128	3.248
34	5.007	1.625	3.820	0.498	1.979	3.227
521	0.709	0.337	NA	NA	1.218	3.027
95	6.861	2.966	4.180	0.795	1.826	3.016
247	1.113	0.516	NA	NA	1.821	2.935
505	2.180	0.949	NA	NA	2.297	2.920
74	4.002	0.837	1.350	1.300	2.357	2.667
38	6.028	1.461	3.430	0.754	0.889	2.614
121	6.692	2.547	4.970	0.333	4.710	2.602
211	6.363	2.268	3.250	1.460	2.048	2.595

Table 15: Asteroid masses obtained with INPOP17a and compared with values extracted from [3] and [8]. Column 7 gives the value of this maximum impact of each asteroid on the Earth-Mars distances as defined in [12].

IAU designation	INPOP17a $\times 10^{-18}$ kg	1- σ $\times 10^{-18}$ kg	Carry 2012 $\times 10^{-18}$ kg	1- σ $\times 10^{-18}$ kg	DE430 $\times 10^{-18}$ kg	Impact km
345	3.534	1.159	NA	NA	0.828	2.561
209	5.328	3.170	NA	NA	1.743	2.529
895	11.986	4.120	NA	NA	2.545	2.470
690	3.734	1.668	2.190	0.994	3.202	2.470
386	12.236	2.055	8.140	1.580	10.135	2.337
93	12.730	1.311	3.350	0.540	3.796	2.247
304	1.274	0.741	NA	NA	0.463	2.229
87	82.787	4.944	14.900	0.733	14.782	2.222
760	1.302	0.887	NA	NA	0.391	2.208
135	1.617	0.938	1.210	0.157	0.640	2.130
471	7.082	1.785	NA	NA	5.686	2.065
702	2.734	1.526	6.060	3.600	5.979	2.009
69	8.970	1.866	7.000	1.900	3.458	2.005
141	8.307	0.933	NA	NA	2.531	1.999
804	1.602	0.809	4.380	1.630	1.524	1.919
91	0.607	0.298	NA	NA	1.640	1.858
241	15.821	3.267	NA	NA	2.020	1.793
790	16.205	5.310	7.520	2.560	11.802	1.791
786	3.487	2.460	NA	NA	1.064	1.788
308	3.740	1.727	4.770	0.398	4.867	1.785
72	2.169	0.666	NA	NA	0.537	1.767
365	4.184	1.477	NA	NA	0.522	1.613
387	1.030	0.247	1.900	0.637	0.675	1.572
751	4.530	1.100	3.270	0.583	1.209	1.398
914	1.967	0.721	NA	NA	0.277	1.384
674	0.423	0.605	NA	NA	0.967	1.328
667	0.246	0.366	NA	NA	0.611	1.322
266	4.227	2.114	NA	NA	1.238	1.315
117	7.451	2.670	4.540	1.400	3.005	1.156
57	5.291	2.167	NA	NA	2.474	1.106
75	0.080	0.114	NA	NA	0.293	1.058
92	1.322	1.920	NA	NA	2.713	1.038
47	1.986	1.365	3.250	1.680	3.726	1.012

- [16] K. Matsuo, B. F. Chao, T. Otsubo, and K. Heki. Accelerated ice mass depletion revealed by low-degree gravity field from satellite laser ranging: Greenland, 1991-2011. Geophys. Res. Lett., 40:4662–4667, September 2013.
- [17] Erwan Mazarico, Michael K. Barker, Gregory A. Neumann, Maria T. Zuber, and David E. Smith. Detection of the lunar body tide by the Lunar Orbiter Laser Altimeter. Geophysical Research Letters, 41(7):2282–2288, 2014.
- [18] Eric L Michelsen. Normal Point Generation and First Photon Bias Correction in APOLLO Lunar Laser Ranging.
- [19] T. Morley. MEX and VEX data release, 2012. Private communication.
- [20] T. D. Moyer. Formulation for Observed and Computed Values of Deep Space Network Data Types for Navigation, volume 2. John Wiley & Sons, Inc., Hoboken, NJ, USA, jan 2003.
- [21] T. W. Murphy, E. G. Adelberger, J. B R Battat, C. D. Hoyle, N. H. Johnson, R. J. McMillan, E. L. Michelsen, C. W. Stubbs, and H. E. Swanson. Laser ranging to the lost Lunokhod 1 reflector. Icarus, 211(2):1103–1108, 2011.
- [22] T. W. Murphy, R. J. McMillan, N. H. Johnson, and S. D. Goodrow. Lunar eclipse observations reveal anomalous thermal performance of Apollo reflectors. Icarus, 231:183–192, 2014.
- [23] T. W. Murphy, Jr., E. G. Adelberger, J. B. R. Battat, C. D. Hoyle, N. H. Johnson, R. J. McMillan, C. W. Stubbs, and H. E. Swanson. APOLLO: millimeter lunar laser ranging. Classical and Quantum Gravity, 29(18):184005, September 2012.
- [24] Thomas W. Murphy and Scott D. Goodrow. Polarization and far-field diffraction patterns of total internal reflection corner cubes. Applied Optics, 52(2):117, jan 2013.
- [25] K. Nordtvedt. Optimizing the observation schedule for tests of gravity in lunar laser ranging and similar experiments. Classical and Quantum Gravity, 15:3363–3381, November 1998.
- [26] Dmitry A. Pavlov, James G. Williams, and Vladimir V. Suvorkin. Determining parameters of Moon’s orbital and rotational motion from LLR observations using GRAIL and IERS-recommended models. Celestial Mechanics and Dynamical Astronomy, 126(1-3):61–88, 2016.
- [27] M.R. Pearlman, J.J. Degnan, and J.M. Bosworth. The International Laser Ranging Service. Advances in Space Research, 30(2):135–143, jul 2002.
- [28] R. Peron. On the use of combinations of laser-ranged satellites orbital residuals to test relativistic effects around Earth. MNRAS, 432:2591–2595, July 2013.
- [29] G Petit and B Luzum. IERS Conventions (2010). IERS Technical Note, 36, 2010.
- [30] J C Ries, Claudio Paris, Richard Matzner, Phuc Nguyen, Jason Brooks, Ignazio Ciufolini, Antonio Paolozzi, and Erricos C Pavlis. LARES Satellite Thermal Forces and a Test of General Relativity LARES Satellite Thermal Forces and a Test of General Relativity. (July), 2016.
- [31] E Myles Standish, James G Williams, and Fundamental Ephemerides. Orbital Ephemerides of the Sun, Moon, and Planets. Tensor, pages 1–33, 2003.

- [32] V. Viswanathan, A. Fienga, C. Courde, J.-M. Torre, P. Exertier, E. Samain, D. Feraudy, D. Albanese, M. Aymar, H. Mariey, H. Viot, and G. Martinot-Lagarde. LLR data analysis and impact on lunar dynamics from recent developments at OCA LLR Station. In EGU General Assembly Conference Abstracts, volume 18 of EGU General Assembly Conference Abstracts, page 13995, April 2016.
- [33] Vishnu Viswanathan, Agnes Fienga, Jacques Laskar, Herve Manche, Jean-Marie Torre, Clément Courde, and Pierre Exertier. Utilizing the Lunar Laser Ranging datasets alongside the radio-science data from the Lunar Reconnaissance Orbiter to improve the dynamical model of the Moon. IAU General Assembly, 22:28567, 2015.
- [34] James G Williams and Dale H Boggs. Secular tidal changes in lunar orbit and Earth rotation. Celestial Mechanics and Dynamical Astronomy, 126(1-3):89–129, 2016.
- [35] James G. Williams, Dale H. Boggs, Charles F. Yoder, J. Todd Ratcliff, and Jean O. Dickey. Lunar rotational dissipation in solid body and molten core. Journal of Geophysical Research, 106(E11):27933, 2001.
- [36] James G. Williams, Slava G. Turishev, and Dale H. Boggs. Lunar laser ranging tests of the equivalence principle with the earth and moon. International Journal of Modern Physics D, 18(07):1129–1175, jul 2009.